International Journal of Robotics and Control Systems
Vol. 6, No. 4, 2026, pp. 2991-3022
ISSN 2775-2658
http://pubs2.ascee.org/index.php/ijrcs

Embedded Comparative Evaluation of PID, $H\infty$ and Hybrid $H\infty$-PID for SCORBOT-ER 4U Joint Setpoint Tracking

Martinus Bagus Wicaksono [a,1], Dechrit Maneetham [a,2,*], Petrus Sutyasadi [b,3]

[a] Department of Mechatronics Engineering, Rajamangala University of Technology Thanyaburi (RMUTT), Pathum Thani 12120, Thailand
[b] Department of Mechatronics Engineering Technology, Sanata Dharma University, Yogyakarta 55282, Indonesia
[1] martinus_b@mail.rmutt.ac.th; [2] dechrit_m@rmutt.ac.th; [3] peter@usd.ac.id
* Corresponding Author

ARTICLE INFO

Article history
Received May 20, 2026
Revised July 07, 2026
Accepted August 13, 2026

Keywords
Hybrid $H\infty$-PID Control;
Embedded Robotic Control;
Setpoint Tracking;
SCORBOT-ER 4U;
Particle Swarm Optimization

ABSTRACT

Joint-level control of embedded robotic manipulators is affected by sampling time, actuator limits, encoder resolution, friction, and backlash, which can change tracking accuracy and control effort. This study implements and compares fixed-parameter PID, $H\infty$, and hybrid $H\infty$-PID controllers for Joint 3 setpoint tracking of the SCORBOT-ER 4U using an ESP32-S3 platform. The contribution is a bounded simulation and hardware comparison under identical embedded test conditions, not a claim that the controllers were tuned by the same procedure. A reduced-order joint model was used for controller design and deterministic simulation. PID gains were obtained offline using PSO with 40 particles and 100 iterations. The $H\infty$ controller was synthesized using mixed sensitivity, with $\gamma = 20.052$. The hybrid controller included PID and $H\infty$ voltage commands utilizing fixed parameters $e_{sw} = 0.25$ rad, a = 10, $\beta = 0.3$, and $\lambda = 0.2$. Simulation and hardware tests used step inputs of ±10°, ±25°, and ±45°, with reduced-order disturbance tests up to 0.50 N·m. In simulation, PID achieved the lowest RMSE, increasing from 0.0606 to about 0.068 rad, but required the highest control energy, about 5.70 V^2·s; $H\infty$ required the lowest energy, below 1.93 V^2·s, but showed slower correction. In hardware tests, the best controller changed with step direction and metric; in large-step responses, the hybrid controller reduced peak overshoot from about 5-7° to 2-3°. The results indicate metric-dependent trade-offs, and no statistical superiority is claimed.

1. Introduction

Robotic manipulators are effectively deployed in a wide range of industrial automation, as well as educational and research settings, where high-accuracy setpoint tracking and reliable joint-level control are required for pick-and-place tasks, welding, material handling, and many other applications [1]–[3]. The SCORBOT-ER 4U five DOF arm has become a realistic testbed among educational robotic platforms, since it is representative of inherently practical control challenges, such as nonlinear joint dynamics, coupling effects, modeling uncertainties, and sensitivity to external disturbances [4], [5]. The control systems of the platforms have to meet operational requirements for precise setpoint tracking over the lifespan of the platforms, while preserving system performance in nonideal conditions. The development of controllers that can handle both modelling uncertainties and external disturbances remains an ongoing research area in control engineering. In practical electromechanical systems, model errors and external disturbances cannot be avoided. For this reason, observer-based and robust controllers have been used to improve tracking under nonideal conditions [6], [7]. When the controller is moved to embedded hardware, other issues also appear. Processor speed, memory, sampling time, and input-output timing can affect the real-time response [8]–[13]. In this work, these embedded aspects are included as part of the comparison condition, not treated only as a programming detail.

Proportional-Integral-Derivative (PID) was selected as the main reference controller because it is simple and commonly used in industrial and laboratory control systems [14], [15]. Its performance, however, can change when the joint model is not accurate, the payload changes, or the joint receives disturbance [16], [17]. Robust methods such as sliding-mode control have been used in DC motor and mechatronic systems to reduce these disturbance effects [18]–[20]. In practice, the benefit must be balanced with implementation difficulty, especially for a low-cost microcontroller. H∞ control gives a more systematic robustness-oriented design [21], [22], but the weighting selection and controller order can make embedded implementation more demanding [23], [24]. Hybrid control is used here as a practical option, by combining PID regulation and H∞ action [25]. GA, ACO, and PSO have also been used to tune controller parameters [26]–[32]. In this paper, PSO is only used to set the PID baseline, while the main comparison is made after PID, H∞, and hybrid H∞-PID are run under the same embedded test setup.

Several studies have reported sliding-mode, computed-torque, and adaptive controllers for robotic and mechatronic systems. These approaches can improve disturbance handling, but not all of them are straightforward for embedded use because some are tested mainly in simulation or require more complex computation. Table 1 provides a summary of representative methods. This table is used to position the present work within the broader robust-control literature and to show that practical embedded validation is still limited in several related studies.

Table 1. Representative Robust Control Strategies in Robotics and Related Systems

System/Platform	Control Strategy	Key Findings	Remarks
Valve-cylinder (hydraulic)	ESMO + Robust SMC	60% error reduction, overshoot minimized	Some chattering remains [33]
2-link manipulator	Robustified CTC (Lyapunov)	Lower Integral Absolute Error (IAE) vs standard (simulations)	Simulation only [34]
2-DOF manipulator	Noise-free robust linear control	Robust tracking, no chattering	Requires high-gain tuning [35]

H∞ and hybrid control strategies have been further researched in robotics often in conjunction with optimization techniques like PSO. These approaches have been shown to improve tracking performance and robustness for a wide variety of applications. However, most implementations are based on simulation or high-performance hardware, with limited validation on embedded robotic platforms. Representative methods are summarized in Table 2. Although these approaches demonstrate improved robustness and tracking performance, they often involve trade-offs such as increased computational complexity, sensitivity to model accuracy, or limited validation under real-time embedded conditions. The studies in Table 2 are the closest to the present work because they involve *H*∞, hybrid robust control, PSO-based robust design, or robotic-arm control; however, they do not provide the same single-joint embedded comparison of PID, *H*∞, and hybrid *H*∞-PID controllers on the SCORBOT-ER 4U under identical hardware and sampling conditions.

Despite these developments, limited studies have systematically evaluated and compared different control strategies under identical real-time embedded conditions, particularly on practical robotic platforms. In this study, identical embedded conditions refer to the same SCORBOT-ER 4U Joint 3, ESP32-S3 controller, BTS7960 motor driver, encoder feedback, 10 ms sampling period, actuator voltage limit, reference inputs, and performance metrics for all tested controllers. Building on earlier studies in robust and hybrid control, this work implements a PSO-tuned hybrid $H\infty$-PID controller for setpoint tracking on the SCORBOT-ER 4U. The scope is intentionally limited to single-joint setpoint tracking using step inputs, rather than full multi-joint trajectory tracking. In contrast to other studies, this study focuses on a unified experimental evaluation of PID, $H\infty$, and hybrid $H\infty$-PID controllers under the same embedded implementation constraints. The hybrid controller combines the disturbance-rejection capability of $H\infty$ control with the simplicity of PID regulation through an error-dependent blending mechanism. PSO is used to determine a fixed set of PID gains prior to simulation and experimental evaluation. All controllers are implemented and tested in real-time on the SCORBOT-ER 4U platform with an ESP32-S3 microcontroller. This implementation highlights the impact of real-world constraints, such as limited sampling time and hardware limitations, on the performance of controllers. The novelty therefore lies mainly in the embedded comparative evaluation under identical practical conditions, supported by SCORBOT-ER 4U hardware validation, rather than in proposing a new $H\infty$ theory or a new PSO algorithm.

Table 2. Representative H∞ and Hybrid Robust Control Strategies in Robotics

System/Platform	Control Strategy	Key Findings	Remarks
Two-link arm	Hybrid PD-$H\infty$.	Improved tracking vs standalone PD/$H\infty$.	Limited to low-DOF [36]
Industrial robot (KUKA machining)	$H\infty$-optimized inertial actuators.	58-91% vibration reduction, 85% machining error reduction.	Robust to pose variations [37]
Quadruped robot	PSO-based structure-specified mixed H2/$H\infty$.	Stable push-recovery under lateral impact, low-order robust controller.	Validated experimentally embedded friendly design [38]
Robotic arm	PSO-based low-order $H_2/H\infty$ PID.	Robust under uncertainties, hardware-proven.	Strong baseline for SCORBOT [39]
Delta parallel robot	Fractional-order sliding mode control	Robust trajectory tracking under disturbances, noise, and payload variation	Journal validation on Delta robot model [40]

In one of our previous works, the approach empirically using hybrid PID-Iterative Learning Control (PID-ILC) for the SCORBOT-ER 4U manipulator in performing repetitive motion with a change of payload, has been verified. Iterative learning reduces the steady-state peak error but requires repetition and is at best inappropriate for any real-time application that requires response during disturbances [41]. This previous work supports the practical relevance of the SCORBOT-ER 4U platform, but the present study addresses a different problem: non-iterative single-joint setpoint tracking using PID, $H\infty$, and hybrid $H\infty$-PID controllers under the same embedded implementation conditions.

In particular, there is still limited experimental and practical evidence of the influence that practical factors such as finite sampling time, actuator saturation, encoder resolution and mechanical nonlinearities have on the performance of a controller when implemented on embedded robotic systems [42]. This is the motivation of the present study. This work is about the implementation and evaluation of different control strategies on an embedded robotic platform under practical constraints. In particular, PID, $H\infty$ and hybrid $H\infty$-PID controllers are implemented and tested in real-time on the SCORBOT-ER 4U robotic system using an ESP32-S3 microcontroller. The main contribution is the embedded hardware comparison. PID, H∞, and hybrid H∞-PID are tested on the same SCORBOT-ER 4U joint, and the comparison is based on tracking error, transient response, and voltage-based control effort. Based on this framework, the main contributions of this study are summarized as follows:

1) Real-time embedded implementation of PID, $H\infty$ and hybrid $H\infty$-PID controllers for Joint 3 of the SCORBOT-ER 4U using an ESP32-S3 platform.
2) A quantitative comparison of the controller performance under the same sampling period, actuator constraints, encoder feedback, reference inputs, and evaluation metrics.

3) Experimental validation of a PSO-tuned hybrid $H\infty$-PID control scheme as a practical compromise controller for setpoint tracking, not as a controller that is superior in every performance metric.

The rest of the paper is organized as follows. Section 2, Method, describes the modelling framework and the design of the controller. Section 3, Results and Discussion, presents simulation and experimental results. Section 4, Conclusion, concludes the paper and outlines future work.

2. Method

The method in this study was arranged in four main stages: system modelling, controller design, simulation, and hardware testing. These stages were used so that PID, $H\infty$, and hybrid $H\infty$-PID controllers could be compared under the same basic conditions. The reduced-order joint model, sampling period, actuator voltage limit, reference inputs, and performance metrics were kept the same for all controllers. By using this arrangement, the comparison could be performed more consistently and the implementation process could be repeated more easily.

Fig. 1 summarizes the flow of this work. Step inputs of ±10°, ±25°, and ±45° are given to the PSO-tuned PID, discrete $H\infty$, and hybrid $H\infty$-PID controllers. After that, the same controllers are checked in simulation and then implemented on the ESP32-S3 connected to Joint 3 of the SCORBOT-ER 4U. The measured responses are compared using RMSE, IAE, and voltage-based control energy, so the test conditions remain the same for the three controllers.

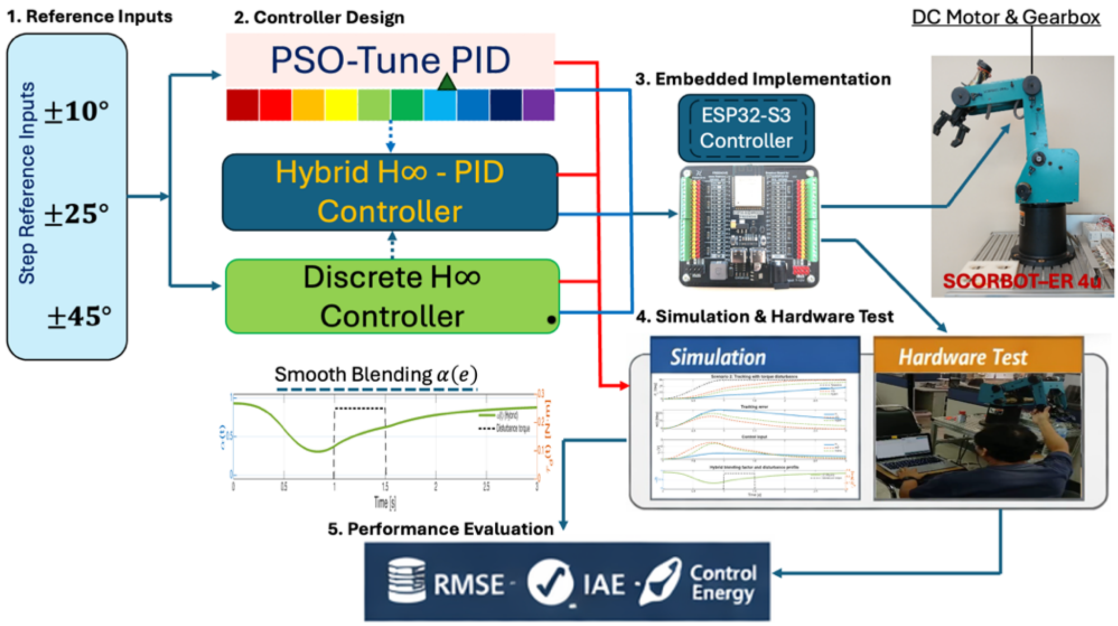

Fig. 1. Research framework for comparing PID, H∞, and hybrid H∞-PID controllers on SCORBOT-ER 4U Joint 3

2.1. System Overview

Fig. 2 shows the SCORBOT-ER 4U platform used for hardware testing. Joint 3 was used because its motion is easier to isolate for a single-joint comparison, while the test still includes real effects from the gearbox, friction, backlash, and actuator limit. The joint uses a brushed DC motor, a high-ratio gearbox, and a BTS7960 motor driver.

The gearbox ratio is approximately 127.7:1. With this ratio, the motor torque is increased at the joint side and the effect of other joints becomes smaller in this experiment. Therefore, Joint 3 is treated as a decoupled joint for controller design. This simplification does not remove gearbox effects.

Friction and backlash still appear in the hardware response, and they are treated here as practical nonidealities, not as separate compensation terms.

The joint position is measured using an incremental encoder mounted on the motor shaft. After calibration, the effective resolution is approximately 41.51 counts per degree. The control algorithm is executed on the ESP32-S3 with a fixed sampling time of 10 ms. In each sampling period, the controller reads the encoder feedback and calculates the control signal for the motor driver.

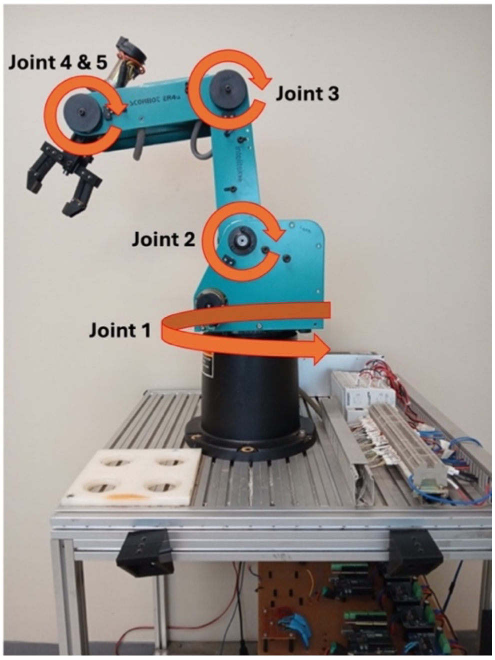

Fig. 2. The joints of SCORBOT-ER 4U

2.2. System Modelling

2.2.1. Full Electromechanical Model

The joint dynamics are described by combining electrical and mechanical subsystems. The electrical dynamics follow the standard DC motor model, where the applied voltage is related to armature resistance, inductance, and back electromotive force.

The electrical dynamics of the DC motor can be expressed as

$$V(t) = Ri(t) + L\left(\frac{di(t)}{dt}\right) + e_b(t) \tag{1}$$

where $V(t)$ is the applied voltage, R and L denote the armature resistance and inductance, respectively, and $e_b(t)$ represents the back electromotive force. The back-EMF is proportional to the angular velocity of the motor shaft,

$$e_b(t) = K_b\omega(t) \tag{2}$$

where $\omega(t) = \frac{d\theta(t)}{dt}$ is the angular velocity, and K_b is the back-EMF constant. The generated motor torque is given by

$$T(t) = K_t i(t) \tag{3}$$

where K_t is the torque constant. This torque is transferred through the gearbox to the joint, which is affected by the inertia and viscous friction and external disturbances. The electrical and mechanical parameters used in this study are obtained from system identification and are summarized in Table 3.

Table 3. Identified Electrical and Mechanical Parameters of the SCORBOT-ER 4U Joint

Symbol	Description	Value	Unit
R	Armature resistance	10.92	Ω
L	Armature inductance	6.2	mH
K_t	Torque constant	0.0396	$N \cdot m/A$
K_b	Back-EMF constant	0.0408	$V \cdot s/rad$
J_{eq}	Equivalent load inertia	0.01	$kg \cdot m^2$
B_{eq}	Viscous friction coefficient	0.006	$N \cdot m \cdot s/rad$
N_g	Gear Ratio	127.7	$-$

2.2.2. Reduced-Order Joint Model

The controller design in this work is based on a reduced-order representation of the joint rather than the full electromechanical model. In the SCORBOT-ER 4U Joint 3 actuator, the electrical dynamics settle much faster than the mechanical motion. At the 10 *ms* sampling period, the motor current reaches steady state within one sampling interval, while the joint position evolves more slowly, consistent with the time-scale separation commonly observed between electrical and mechanical dynamics in DC motor systems [43], [44]. Based on the identified motor parameters, the electrical time constant is approximately $L/R = 6.2\ \text{mH}/10.92\Omega \approx 0.57\ \text{ms}$**,** which is much smaller than the 10 ms sampling period. This supports the reduced-order assumption for the dominant joint-motion analysis. Thus, the electrical dynamics are of little importance for the dominant low frequency joint motion considered in this study.

Therefore, the electrical states have a limited influence on the dominant joint response and can be neglected for control design. The joint dynamics can be approximated by a second-order mechanical model,

$$J_{eq} = \ddot{\theta}(t) + B_{eq}\dot{\theta}(t) = K_u u(t) - \tau_d(t) \tag{4}$$

where J_{eq} and B_{eq} denote the equivalent inertia and viscous friction, $u(t)$ is the control input (voltage), and $\tau_d(t)$ represents the combined effect of gravitational loading, friction asymmetry, backlash, and other unmodeled disturbances [45]. The gain K_u represents the motor and gearbox effects referred to the joint side.

This simplified model captures the dominant mechanical behavior while remaining suitable for real-time implementation on the ESP32-S3. Nonlinear effects such as friction asymmetry, backlash, gravity-related bias, encoder quantization, and actuator saturation are not explicitly modelled in the controller design. Instead, these effects are treated as unmodelled disturbances and practical hardware constraints whose influence is evaluated through real-time experiments. Thus, the reduced-order model is used for controller synthesis and comparison, while the hardware tests are used to reveal the effect of nonideal implementation conditions.

For digital implementation, the model is discretized with a sampling period of T_s= 10 *ms* using the Tustin approximation, yielding

$$x(k+1) = A_d\, x(k) + B_d\, u(k) \tag{5}$$

$$y(k) = C_d\, x(k) \tag{6}$$

where the state vector consists of the joint angle and angular velocity, and (A_d, B_d, C_d) are derived from the continuous model. This format is utilized uniformly for all controllers in this investigation. The reduced-order model allows us to construct the controller and conduct experimental validation on the embedded platform in a practical manner.

2.3. Controller Design

2.3.1. PSO-Tuned PID Controller

In this work, the PID controller is utilized as a reference mainly to compare it with the *H*∞ and hybrid *H*∞-PID controllers. The PID gains (K_p, K_i, K_d) are not manually tuned but derived offline by a Particle Swarm Optimization (PSO) process based on the reduced-order joint model in Section 2.2.2. After the PSO process is completed, the obtained PID gains are fixed and used unchanged in all simulations and hardware experiments. The final optimized PID gains are reported in Table 4.

Table 4. PSO Parameter Settings and Optimized PID Gains

Parameter	Value
Swarm size	40 particles
Number of iterations	100 iterations
Inertia weight (w)	0.72
Cognitive coefficient c_1	1.5
Social coefficient c_2	1.5
K_p search bound	0 to 200
K_i search bound	0.704 to 500
K_d search bound	0 to 5
Objective function	ITAE-based cost function
Stopping Criterion	Fixed maximum number of iterations
Number of independent PSO runs	1 deterministic run with fixed random seed
Final K_p	9.0526
Final K_i	0.7040
Final K_d	1.4907

In practice it tests different combinations of gain within given boundaries. The closed-loop response for each gain-set is simulated using the same reference signals that are subsequently employed in both simulation and experimental tests. This guarantees that the tuning circumstances are the same as the ones under which the controller will actually be evaluated.

The performance of each candidate is evaluated by the Integral of Time-weighted Absolute Error (ITAE),

$$J = \sum_{k=0}^{N} k\,|e(k)| \tag{7}$$

where $e(k)$ is the tracking error. ITAE is more sensitive to errors in time than simpler error measures, while still allowing a short transient response. This is suitable for the type of joint motion considered in this work [46]. The numerical settings of the PSO routine and the final optimized PID gains are summarized in Table 4. The PSO was performed offline using a fixed random seed to ensure reproducibility. The optimization itself is not claimed as a new algorithmic contribution but is used to obtain a consistent PID baseline for evaluating the *H*∞ and Hybrid *H*∞-PID controllers. Because only one deterministic PSO run with a fixed random seed was used, robustness of the optimized gains to different random initializations was not formally evaluated in this study.

The tuning process itself follows the standard PSO procedure, as illustrated in Fig. 3. The particles are first initialized randomly within the gain limits. During each iteration, the closed-loop response is evaluated, and both the individual best and global best solutions are updated. The particle velocities and positions are then updated based on the inertia, cognitive, and social terms. The findings indicate that the particles move towards better regions in the search space. This iteration is repeated a fixed number of times.

The update equations follow the standard PSO formulation [28], [46],

$$v_i^{k+1} = w\,v_i^k + c_1 r_1\left(p_i^{best} - x_i^k\right) + c_2 r_2\left(g^{best} - x_i^k\right) \tag{8}$$

$$x_i^{k+1} = x_i^k + v_i^{k+1} \tag{9}$$

where x_i^k represents the candidate PID gain vector of particle i and v_i^k its velocity at iteration k. The terms p_i^{best} and g^{best} denote the best solutions found by the particle and the swarm, respectively [47]. The coefficients are selected to balance exploration and convergence.

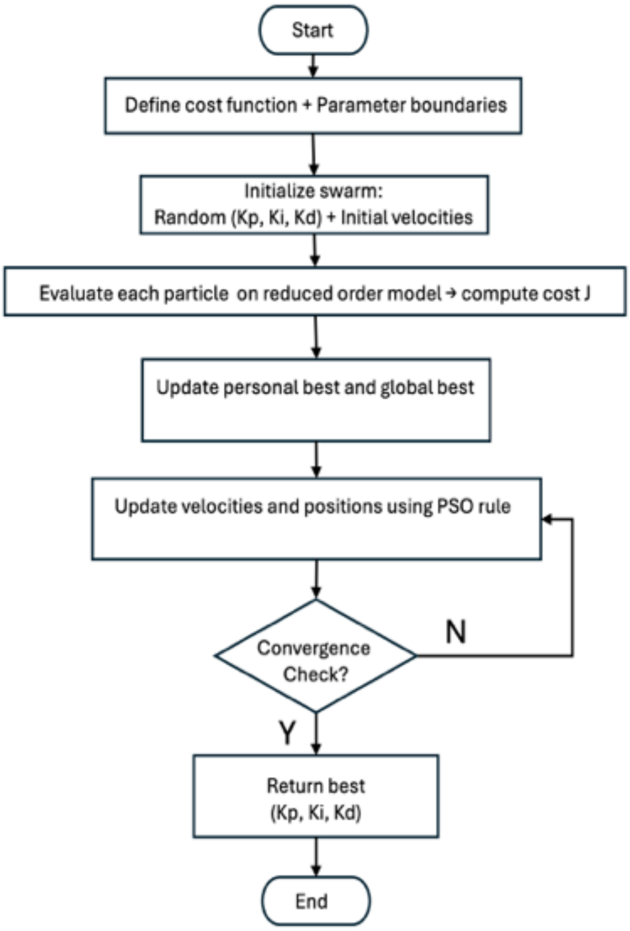

Fig. 3. Flow of the PSO-based PID gain tuning procedure

Fig. 4 illustrates that the particle distribution changes during the optimization process. Initially, because of random initialization, the particles are spread over a rather large area. In contrast, as the iterations progress, the particles start to congregate within a narrower range, which clearly shows that in this phase analysis the operations are closing on an appropriate set of gains.

The PSO routine was performed offline, and the resulting PID gains are fixed for all simulations and hardware experiments. No online adaptation is applied. In the ESP32-S3 implementation, a first-order low-pass filter is used in the derivative term to reduce encoder noise. PSO was used here only to obtain a consistent and reproducible PID baseline for comparison with the *H*∞ and Hybrid *H*∞-PID controllers.

2.3.2. *H*∞ Controller

The second controller considered in this study is an *H*∞ design based on the reduced-order joint model introduced in Section 2.2.2. In practical operation, the SCORBOT-ER 4U joint exhibits effects that are not fully captured by this simplified model, including direction-dependent friction, backlash, and variations in load conditions. These factors introduce uncertainty in the system dynamics and can degrade the performance of fixed-gain controllers. Robust-control studies for uncertain robotic manipulators also emphasize that model uncertainty and disturbance effects should be considered when evaluating tracking performance [48].

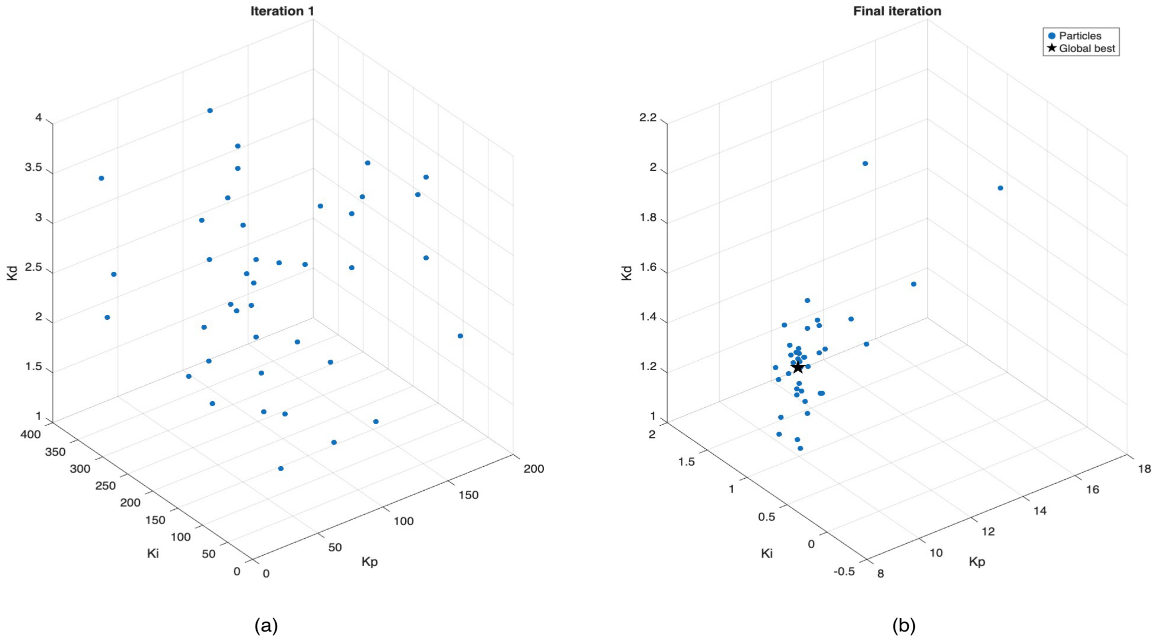

Fig. 4. Distribution of PSO particles in the PID gain space during the tuning process: (a) initial iteration with randomly initialized gains, and (b) final iteration after convergence

To address this issue, an *H∞* controller is employed as a robustness-oriented reference. The objective is to shape the closed-loop response such that the influence of disturbances and model uncertainties on the tracking performance is reduced, while maintaining acceptable control effort [49], [50]. In this study, the term robustness oriented is used in a practical embedded control sense, because the controller is evaluated under disturbance and parameter variation tests rather than through a full formal robust-stability proof of the complete nonlinear hardware system.

The controller design is based on a mixed-sensitivity structure where weighting functions are assigned to the tracking error, control effort and output angle channels. This structure allows the relative importance of tracking accuracy, voltage demand, and output limitation to be adjusted according to the requirements of the joint-control system.

The overall configuration is based on the typical mixed-sensitivity *H∞* architecture as shown in Fig. 5. In this form the weighting functions are selected to minimize tracking error at low frequencies, to avoid unnecessary control activity, and to limit the impacts of high frequency noise and unmodeled dynamics. This formulation serves as the basis for the controller synthesis and implementation described in the subsequent subsections [51]–[55].

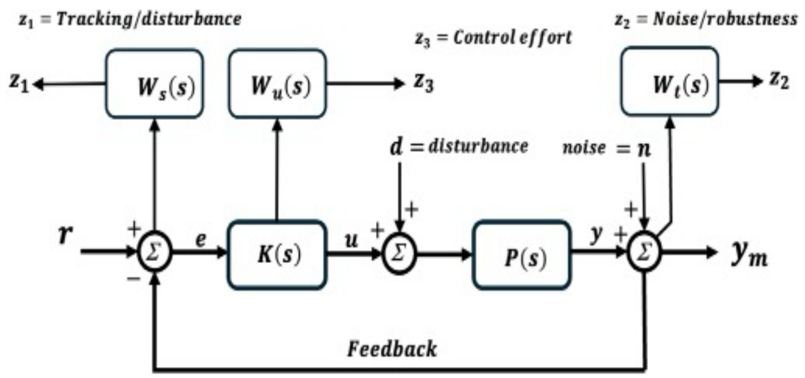

Fig. 5. Mixed sensitivity H∞ control structure used in this study

2.3.3. Weight Selection

The $H\infty$ controller is formulated using a generalized plant in which performance is shaped by scalar weights applied to the tracking error, control effort, and output angle. The weighted performance outputs are grouped into the performance vector **z**, as defined in (10). The weighted performance vector is expressed as

$$z = \begin{bmatrix} z_1 \\ z_2 \\ z_3 \end{bmatrix} = \begin{bmatrix} W_s(r-y) \\ W_u u \\ W_e y \end{bmatrix} \tag{10}$$

where r is the reference input, y is the joint-angle output, and u is the motor-voltage command. In (10), $W_s(r-y)$ represents the tracking-error channel, $W_u u$ represents the control-effort channel, and $W_e y$ represents the output-angle channel. The weights are chosen as constant values. This keeps the design simple and fits the reduced-order model used in this embedded comparison.

Starting from unity weights, several scalar combinations were checked on the reduced-order model. The selected values were $W_s = 20, W_u = 0.1$, and $W_e = 1$. During this process, the closed-loop response, voltage demand, and numerical conditioning were observed. Weight combinations that produced very slow tracking, too much control activity, or synthesis problems were not used.

With this selection, W_s gives stronger emphasis to tracking error and low-frequency disturbance rejection. W_u is used to avoid an overly aggressive voltage command; the value 0.1 was kept because it remained compatible with the motor-driver limit. W_e is set to 1, so the output-angle channel remains included without dominating the design. The selected $H\infty$ synthesis settings are summarized in Table 5.

Table 5. H∞ Controller Synthesis Settings

Parameter	Value
Synthesis method	MATLAB hinfsyn
Plant type	Continuous-time generalized plant
Measured output, nmeas	1
Control input, ncont	1
Feedback measurement	Tracking error, $e = r - y$
Control signal	Motor voltage command, u
Tracking-error weight, W_s	20
Control-effort weight, W_u	0.1
Output-angle weight, W_e	1
Exogenous inputs	Reference input r and disturbance torque τ_d
Achieved $H\infty$ performance bound, γ_{opt}	20.052
Continuous-time controller order	2
Discretization method	Zero-order hold (ZOH)
Sampling period	10 ms
Online adaptation	No

The surrounding weight values are found to result in similar closed-loop responses and the selected set was fixed when a practical and implementable solution was obtained [51]. The specific weights chosen are determined by the joint dynamics and actuator limits identified. The actual numbers may vary for systems with varied features but the same tuning approach can be used to reach a workable solution.

2.3.4. $H\infty$ Synthesis Procedure

The $H\infty$ controller is synthesized with the mixed-sensitivity formulation to the generalized plant obtained from the reduced-order joint model by fixing the weights. The generalized plant is composed of the reference and the disturbance inputs, the weighted performance outputs, and the measured tracking error as described in the preceding subsection.

The synthesis problem is posed as a minimization of the closed-loop $H\infty$ norm from the exogenous inputs vector w to the weighted performance vector z. In this study, w consists of the reference input and disturbance torque. The task is to find a stabilizing controller $K(s)$ such that

$$\|T_{zw}(s)\|_{\infty} < \gamma \tag{11}$$

where $T_{zw}(s)$ represents the closed-loop transfer function from w to z, and γ is the achieved $H\infty$ performance bound obtained from the synthesis result.

The controller was synthesized in MATLAB using the *hinfsyn* function with one measured output and one control input. The tracking error $e = r - y$ was treated as the measured signal, while the motor voltage command u was treated as the control input. For the selected weights W_s, W_u, and W_e, the synthesis returned the controller $K_{H\infty}$ and the achievable performance value γ_{opt}.

The value of γ_{opt} was not specified beforehand and was not used as a tuning parameter. In this study, it is only reported to verify that the weighted closed-loop problem was solved. It is not used as a performance metric for comparing the PID, $H\infty$, and Hybrid $H\infty$-PID controllers. The resulting continuous-time $H\infty$ controller has a second-order state-space realization, which is comparable to the order of the reduced joint model. This low-order realization is important for implementation on the ESP32-S3 because only two controller states must be updated at each sampling instant. Once synthesized, the controller matrices were fixed and used unchanged in all simulations and hardware experiments.

2.3.5. Discretization and Embedded Implementation

The synthesized $H\infty$ controller is obtained in continuous-time state-space form and discretized for implementation on the ESP32-S3 using the same sampling period as the joint control system, $T_s = 10$ ms. Zero-order hold discretization was used so that the simulation model and embedded controller followed the same sampling condition. The discrete-time controller is expressed as

$$x_K(k+1) = A_{K,d}\, x_K(k) + B_{K,d}\, e(k) \tag{12}$$

$$u_{H\infty}(k) = C_{K,d}\, x_K(k) + D_{K,d}\, e(k) \tag{13}$$

where $x_K(k)$ is the discrete controller state and $e(k)$ is the tracking error. The controller output $u_{H\infty}(k)$ is interpreted as the motor voltage command. During simulation and hardware evaluation, this command is monitored against the allowable ±24 V motor driver limit so that the $H\infty$ controller is compared under the same actuator condition as the other controllers. No additional online adaptation is applied to the $H\infty$ controller. The discretized controller is fixed after synthesis and serves as the robustness-oriented component in the Hybrid $H\infty$-PID scheme. This implementation choice keeps the comparison fair because the PID, $H\infty$, and Hybrid $H\infty$-PID controllers are all evaluated using fixed controller parameters under the same sampling period, reference inputs, actuator limit, and evaluation metrics.

2.3.6. Hybrid *H*∞-PID Controller Design

The third control strategy considered in this study is a hybrid controller that combines the PSO-tuned PID controller with the discrete $H\infty$ controller described in the previous subsections [50]. The aim is to take advantage of the rapid corrective response of the PID controller when severe tracking errors are present, while maintaining the robustness of the $H\infty$ controller when the system is operating near the reference position [56]. In this study, the hybrid scheme is treated as a practical fixed-parameter blending strategy, not as a new H∞ synthesis method, a new PSO algorithm, or a formal robust-stability proof for the complete nonlinear hardware system.

The hybrid controller is structured in parallel, with both controllers acting on the same tracking error signal. The relative contribution of each controller is determined by an error-dependent blending process, where smooth transition between control actions is preferred to reduce abrupt switching effects during transient operation [57], [58]. This enables the control action to switch smoothly between aggressive correction and robust regulation as the operating situation changes. The block diagram of the general structure of the hybrid *H*∞-PID controller is shown in Fig. 6. Both controller branches receive the same tracking error and are evaluated under the same sampling period, actuator-voltage limit, reference inputs, and performance metrics used for the stand-alone PID and *H*∞ controllers.

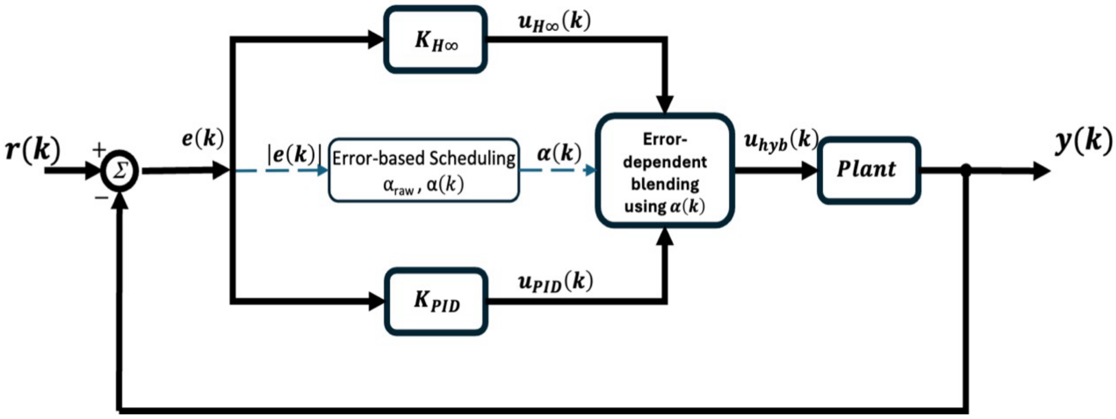

Fig. 6. Structure of the hybrid H∞-PID controller

2.3.7. Hybrid Control Law

The PID and *H*∞ controllers operate in parallel using the same tracking error,

$$e(k) = \theta_{\text{ref}}(k) - \theta_{\text{meas}}(k) \tag{14}$$

and generate the control signals $u_{\text{PID}}(k)$ and $u_{H_\infty}(k)$, respectively. The hybrid control input is defined as a convex combination of these signals,

$$u_{\text{hyb}}(k) = \big(1 - \alpha(k)\big)\, u_{H_\infty}(k) + \alpha(k)\, u_{\text{PID}}(k) \tag{15}$$

where $\alpha(k) \in [0,1]$ is a continuous scheduling parameter. Small values of $\alpha(k)$ emphasize the *H*∞ controller, while larger values boost the contribution of the PID controller. This mixing method prevents sudden changes and guarantees a continuous control signal. The continuous blending formulation is used to avoid abrupt controller switching, which may introduce oscillatory or discontinuous control behavior during transient operation, consistent with practical hybrid-control approaches reported in previous studies [58]–[62]. The scheduling parameter is bounded between 0 and 1, so the resulting command remains a convex combination of the PID and *H*∞ voltage commands.

The embedded implementation employs the same sign convention, PWM voltage conversion, and ±24 V actuator limit for both controller branches, which are expressed as motor-voltage commands prior to merging. The PID and *H*∞ outputs are both interpreted as voltage commands that are sent to the same motor driver interface, and therefore, no additional normalization is applied. The stand-alone PID, stand-alone *H*∞, and hybrid controllers are evaluated consistently by applying friction compensation and torque-bias terms after the blending phase.

2.3.8. Error-Dependent Scheduling and Implementation

The blending factor $\alpha(k)$ is defined as a smooth function of the tracking error magnitude using a sigmoidal mapping,

$$\alpha_{\text{raw}}(k) = \frac{1}{1 + \exp[a(|\,e(k)\,| - e_{\text{sw}})]} \tag{16}$$

where e_{sw} defines the error level at which the transition between controllers occurs, and a controls the sharpness of the transition. This formulation results in larger tracking errors leading to larger $\alpha(k)$, increasing the contribution of the PID controller, whilst smaller errors move the control action towards the $H\infty$ controller. To avoid abrupt switching that may cause oscillatory behavior in the control signal, a sigmoidal function is chosen to offer a smooth and continuous transition between controllers. The transition threshold and sigmoid slope are selected from reduced-order step-response simulations to avoid frequent branch changes near the reference while still allowing PID-dominant correction for larger errors.

To reduce sensitivity to small oscillations near the transition region, $\alpha(k)$ is smoothed using a first-order recursive filter,

$$\alpha(k) = (1-\beta)\,\alpha(k-1) + \beta\,\alpha_{\text{raw}}(k), 0 < \beta \leq 1 \quad (17)$$

where smaller values of β provide smoother but slower variation of the scheduling factor. An additional first-order smoothing stage may be applied to the control signal,

$$u(k) = (1-\lambda)\,u(k-1) + \lambda\,u_{\text{hyb}}(k), 0 < \lambda \leq 1 \quad (18)$$

where λ determines the degree of smoothing, and λ = 1 corresponds to no additional filtering. The smoothing stages are used only to reduce abrupt changes in the scheduling variable and voltage command; they are not used as adaptive retuning mechanisms. Their values are kept moderate to avoid adding unnecessary phase lag to the embedded control loop.

The hybrid controller is implemented on the ESP32-S3 using the same 10 ms sampling period as the individual PID and $H\infty$ controllers. Only the PID integral and derivative states, the $H\infty$ controller states, and the scalar scheduling variable are updated at each sampling instant. The selected hybrid scheduling and smoothing parameters are summarized in Table 6. These parameters were fixed before simulation and experimental evaluation and were used unchanged for all step amplitudes, disturbance cases, and hardware tests. Therefore, the hybrid controller is not an online adaptive controller, and the comparison remains based on fixed controller parameters.

Table 6. Hybrid H∞-PID Scheduling and Smoothing Parameters

Parameter	Function in the Hybrid Controller	Value Used in This Study	Selection Basis
e_{sw}	Error threshold for the transition between $H\infty$-dominant and PID-dominant action	0.25 rad	Selected from reduced-order step-response simulations to define the transition region
a	Sigmoid sharpness parameter	10	Chosen to provide a smooth transition without abrupt controller switching
β	First-order smoothing coefficient for the scheduling factor	0.3	Used to reduce sensitivity to small error oscillations near the transition region
λ	First-order smoothing coefficient for the final control command	0.2	Used only to smooth voltage-command changes; no online retuning is applied

2.4. Simulation Setup

Simulation investigations are performed with the reduced-order discrete-time joint model given in Section 2.2.2 with a sampling period of T_s = 10 ms consistent with the embedded implementation. The complete simulation process is shown in Fig. 7. The simulations were used as a controlled comparison environment to evaluate relative controller behavior before hardware testing, not as a complete representation of all nonlinear effects in the physical joint.

Three controllers, the PSO-tuned PID controller, the $H\infty$ controller and the hybrid $H\infty$-PID controller, are compared under the same conditions. The controller parameters are constant for all simulations. The step inputs of ±10°, ±25° and ±45° are employed to assess the setpoint tracking performance under different operating ranges, which is compatible with the experimental study. The model receives the control signal, and the resulting joint motion is recorded. The controller parameters used in the simulation study and their corresponding source sections are summarized in Table 7. No controller was retuned between step amplitudes, disturbance cases, or hardware tests.

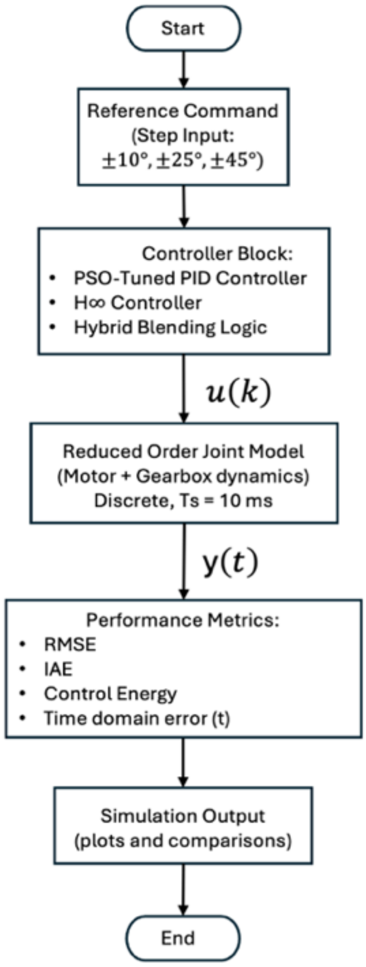

Fig. 7. Simulation flow used to evaluate the PID, H∞, and Hybrid controllers

Table 7. Controller Parameters Used in the Simulation Study and Their Origin

Controller	Parameters Used in Simulation	Source Section in Manuscript	Tuned or Adapted Online
PID	K_p, K_i, K_d	Section 2.3.1 (PSO-Tuned PID Baseline)	No
H∞	Discrete-time controller matrices derived from W_s, W_u, W_t	Section 2.3.2 (*H*∞ Controller and Weight Selection)	No
Hybrid *H*∞-*PID*	$e_{sw}, a, \beta, \lambda$	Section 2.3.3 (Hybrid *H*∞-PID Controller)	No

Robustness is assessed by introducing disturbance torques and variations in the equivalent inertia and damping, while keeping the controller parameters unchanged. These tests are treated as sensitivity tests of the reduced-order model, rather than as a formal robust-stability proof for the complete nonlinear hardware system. Actuator saturation is not explicitly modelled; instead, the control signal is monitored against the ±24 V hardware limit, and no saturation is observed during the simulation runs.

2.5. Experimental Setup

The hardware experiment was carried out on Joint 3 of the SCORBOT-ER 4U under normal laboratory operating conditions. The test setup used an ESP32-S3 microcontroller, a BTS7960 motor driver, and an incremental encoder for joint-position feedback. The PSO-tuned PID controller, the discrete *H*∞ controller, and the hybrid *H*∞-PID controller were implemented on the same ESP32-S3 platform using the fixed parameters listed in **Error! Reference source not found.**. The controller generated PWM signals for the motor driver, while the encoder data were used to estimate the current joint position. The sampling time was set to 10 ms, the same as in the simulation.

Step reference inputs of ±10°, ±25°, and ±45° were used to test the response of the joint at different operating ranges. During the experiment, the reference input, measured joint position, and motor voltage command were recorded for analysis. Joint motion was kept within safe mechanical limits. All controllers were tested using the same sampling period, reference inputs, actuator limits, encoder feedback, and evaluation metrics. The experiments were repeated to check whether the response trend was consistent, but formal statistical confidence intervals were not calculated in this study.

Motor current was also monitored using an ACS712 Hall-effect current sensor during the test. However, the main quantitative comparison in this paper is based on joint-position tracking and voltage-based control effort. The hardware experiment includes real effects such as friction, backlash, actuator limits, and motor-driver behavior, which are not fully represented in the reduced-order simulation model. Similar practical constraints have been reported to affect manipulator tracking performance, especially when input saturation, friction, and state constraints are present [63]–[66]. The hardware wiring used in the experiments is shown in Fig. 8. Therefore, the experimental results are used to observe the behavior of the fixed controllers under practical embedded conditions, while the simulation results are used as a controlled reference for comparison.

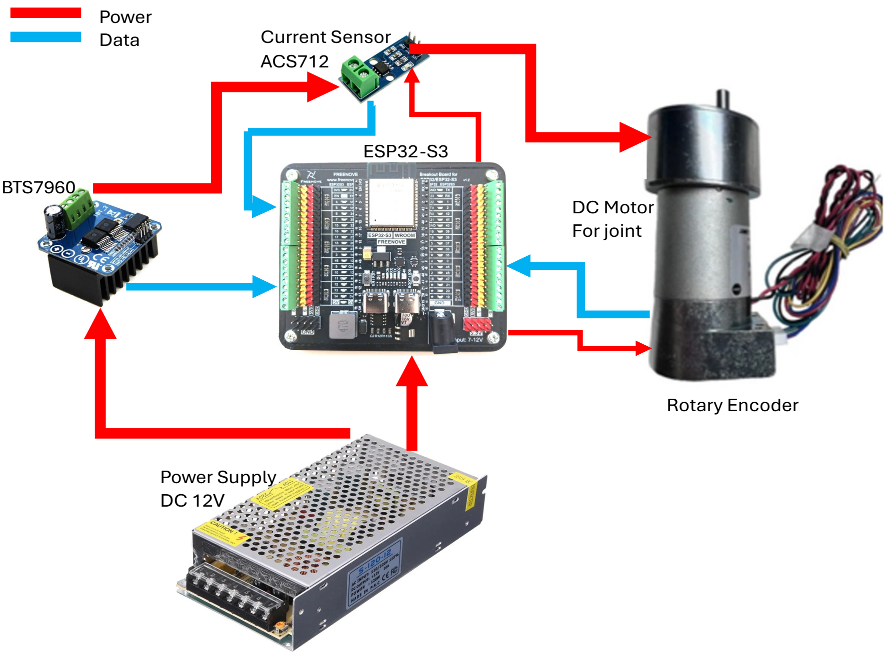

Fig. 8. Wiring diagram of the hardware setup used in the SCORBOT-ER 4U joint experiments

3. Results and Discussion

3.1. Simulation Result

This section presents simulation results obtained using the reduced-order joint model described in Section 2.2.2. The simulations are intended to provide a consistent basis for comparing the three control strategies considered in this study: the PSO-tuned PID controller, the discrete-time $H\infty$ controller, and the hybrid $H\infty$-PID controller. Since the model does not fully include nonlinear hardware effects such as friction asymmetry, backlash, encoder quantization, and actuator dead-zone behavior, the simulation results are interpreted as relative controller-comparison results rather than complete predictions of the experimental response.

All simulations were conducted in discrete time with a sampling period of 10 ms, matching the embedded controller update rate. Controller parameters were defined prior to simulation and remained fixed throughout the study. Nominal tracking performance was evaluated using step inputs of ±10°, ±25°, and ±45°. Additional sensitivity tests were performed by applying disturbance torques and varying the equivalent inertia and damping of the reduced-order model. These tests were used to observe how the fixed controllers respond to non-nominal model conditions, not to claim a formal robust-stability proof for the complete nonlinear hardware system.

Controller performance was evaluated using root-mean-square error (RMSE), integral absolute error (IAE), control energy, and time-domain response characteristics. The same performance measures are used in the experimental analysis to enable direct comparison between simulation and hardware results. However, differences in absolute numerical values between simulation and experiment are expected because the physical joint includes nonlinear and direction dependent effects that are not explicitly represented in the reduced-order model.

3.1.1. PSO-Tuned PID Simulation Results

A PID baseline was established using gains obtained through Particle Swarm Optimization (PSO). These gains were fixed and reused in all subsequent simulations and experiments and serve as a reference for comparison with the $H\infty$ and hybrid controllers. Therefore, the PSO stage is used only to obtain a reproducible PID baseline and is not treated as an online tuning or adaptation mechanism.

The PSO routine was applied to the reduced-order joint model using the ITAE-based objective described in Section 2.3.1. The convergence behavior is shown in Fig. 9. Most of the cost reduction occurs within the first ten iterations, with the objective decreasing from approximately 1.07 to below 0.27. After 15-20 iterations, the cost curve becomes nearly flat, and the cost stabilizes at a final value of $J = 0.2586$. This behavior indicates that the selected gains are obtained after convergence of the offline PSO search for the tested reduced-order model.

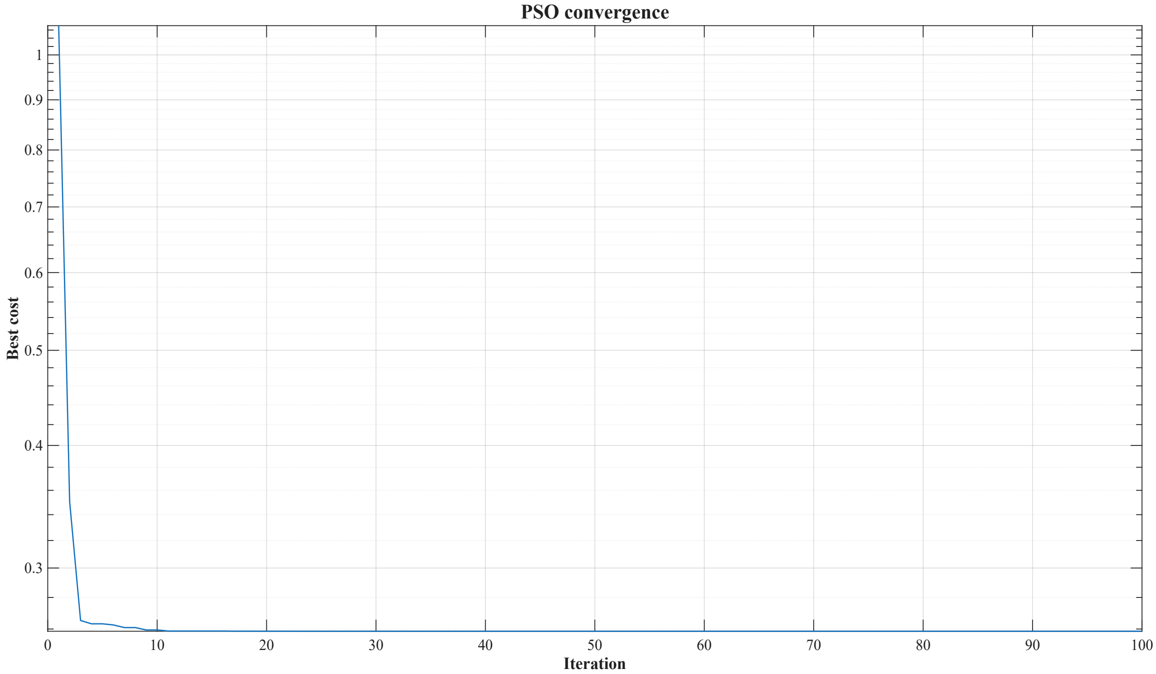

Fig. 9. Convergence of the PSO routine during PID tuning

The resulting PID gains are summarized in Table 8 and were used without modification in all simulation and experimental evaluations. The value of the ITAE component of the cost at the final solution is 0.161, while the steady-state error term is approximately 10^{-3}. This indicates that the optimization mostly affects transient behavior and that the steady-state offset remains small in the reduced-order simulation. Because the same gains are used in all later tests, the PID controller provides a fixed reference case for evaluating the $H\infty$ and hybrid $H\infty$-PID controllers.

Fig. 10 closed-loop step response of the reduced order joint model with the PSO-tuned PID gains. The resulting joint position tracks the reference without visible oscillations in the reduced-order simulation, and the tracking error decreases after the transient. These gains provide a fixed nominal baseline for comparison with the subsequent controllers. The result should be interpreted as a nominal reduced-model response, while the hardware tests are used later to evaluate the effect of physical nonidealities.

Table 8. PSO-Tuned PID Gains

Gain	Value
K_p	9.0526
K_i	0.7040
K_d	1.4907

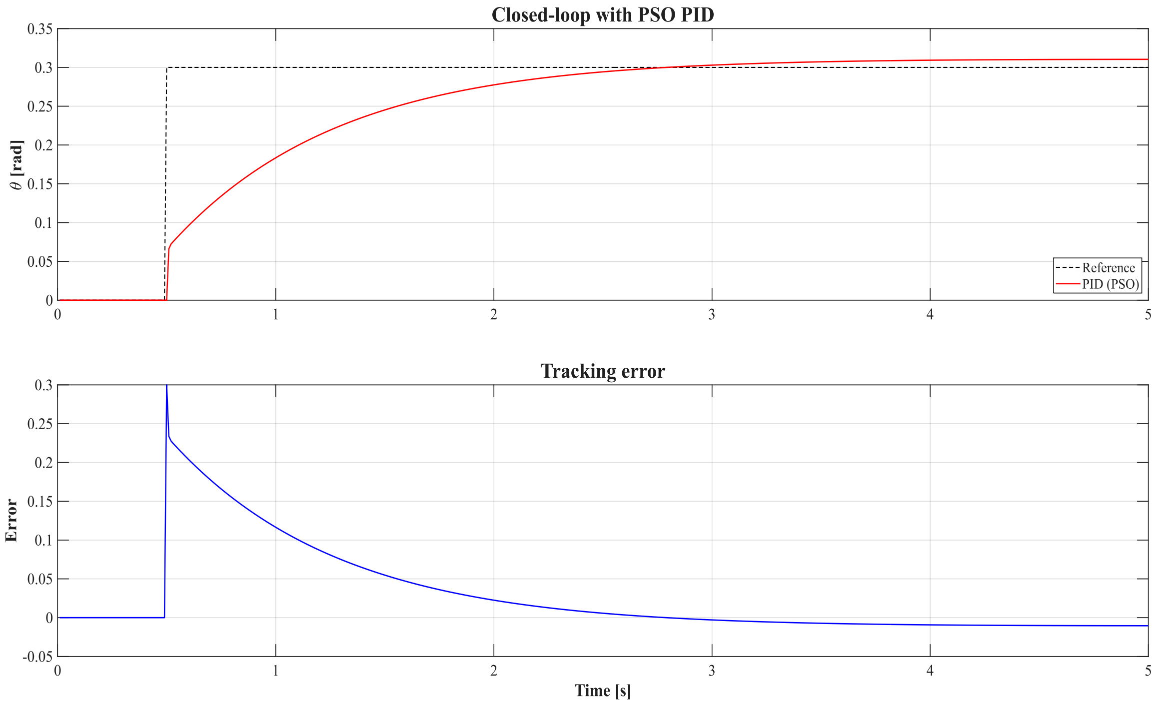

Fig. 10. Closed-loop response of the reduced joint using PSO-tuned PID gains

3.1.2. Nominal Tracking and Disturbance Response

Considered in the specific joint-level configuration, external torque disturbances directly affect the motor-gearbox dynamics and are not compensated by a disturbance observer. Hence their effect is explicitly seen in the closed-loop response. The PID controller is first examined under nominal and bounded-disturbance conditions because it serves as the fixed baseline for the later comparison with the $H\infty$ and hybrid $H\infty$-PID controllers. The disturbance test in this subsection uses a single deterministic torque pulse; a disturbance-amplitude sweep is discussed in the next subsection.

Fig. 11 compares the PID response under nominal condition and under bounded torque disturbance with the maximum magnitude of 0.25 N·m. In the nominal case, the joint follows a 30° step input (≈0.52 rad) and approaches the reference within about 1-1.5 s in the reduced-order simulation. The tracking error decreases after the transient and remains small without visible persistent oscillation.

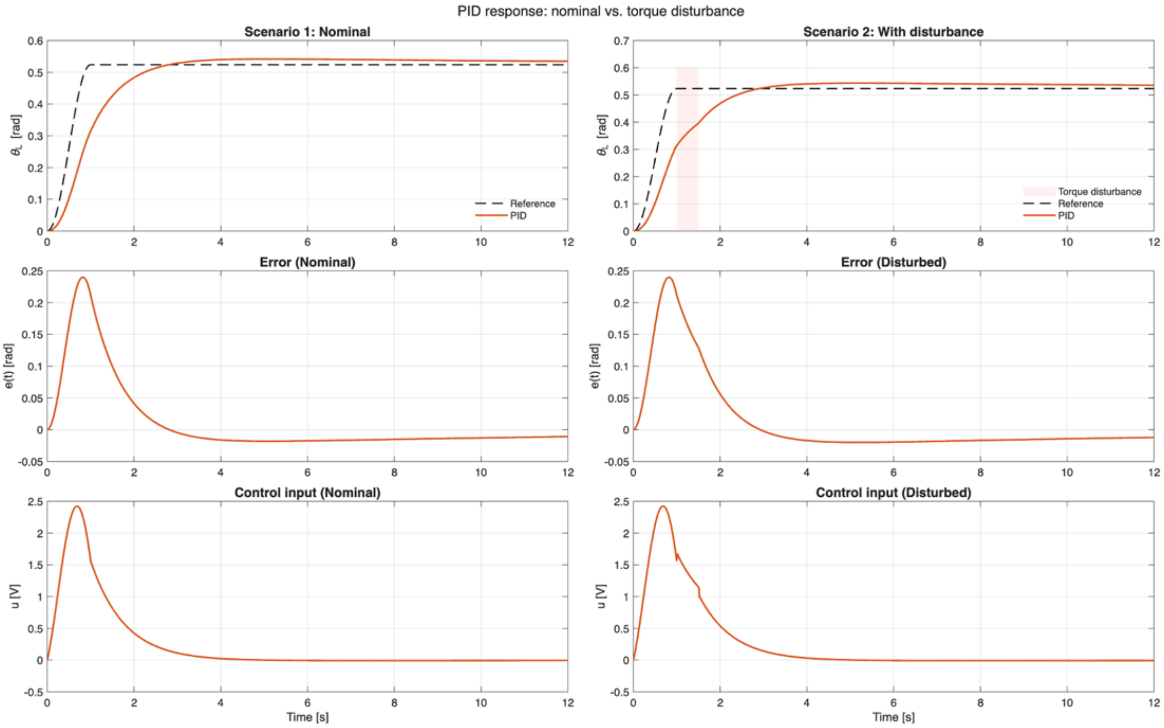

Fig. 11. PID response under nominal and disturbed condition

When the torque disturbance is applied the steady state behavior is similar but the transient deviation is larger and the error decays slower. In the disturbance interval the commanded motor voltage is increased intermittently, indicating a higher control effort. After the disturbance is removed, the joint position gradually returns to the reference. This response shows the expected sensitivity of the PID baseline to an unmeasured external torque disturbance.

Fig. 12 shows the nominal tracking responses of the three controllers for the same 30° step input. The PID controller gives the fastest initial response in this reduced-order simulation, while the *H*∞ controller produces a slower and smoother response with lower control activity. The hybrid response lies between these two behaviors, indicating the intended compromise between fast correction and smoother regulation. This comparison is limited to the nominal reduced-model condition; hardware nonlinearities are evaluated later in the experimental section.

The corresponding control input trends also show the trade-off among the controllers. The PID controller produces the largest actuation peak, the *H*∞ controller gives the smallest command magnitude, and the hybrid controller remains between these responses. This supports using voltage-based control effort as an additional performance measure rather than relying only on tracking error.

Fig. 13 shows the tracking responses of the three controllers in the presence of a bounded torque disturbance. All controllers exhibit larger deviations and slower convergence compared to the disturbance-free case. The PID controller responds fastest at the beginning of the disturbance interval, but this response is accompanied by larger control activity, with the control input reaching about 2-2.5 V in the plotted simulation.

The *H*∞ controller restricts the control activity better, although the transient recovery becomes slower, control signals remaining below about 1.5 V. The hybrid controller reduces the large actuation peaks observed in the PID response while recovering faster than the *H*∞ controller. Therefore, the hybrid result is interpreted as a compromise response for this bounded disturbance simulation, not as evidence that the hybrid controller is superior in every metric or every condition.

Fig. 13(d) displays the evolution of the blending factor, showing a smooth change from PID-dominant to *H*∞-dominant control contributions as the tracking error decreases. The plot shows how the hybrid controller moves from PID-dominant correction during larger errors toward $H\infty$-dominant regulation near the reference. The transition remains continuous, so no abrupt switching command is introduced by the scheduling mechanism.

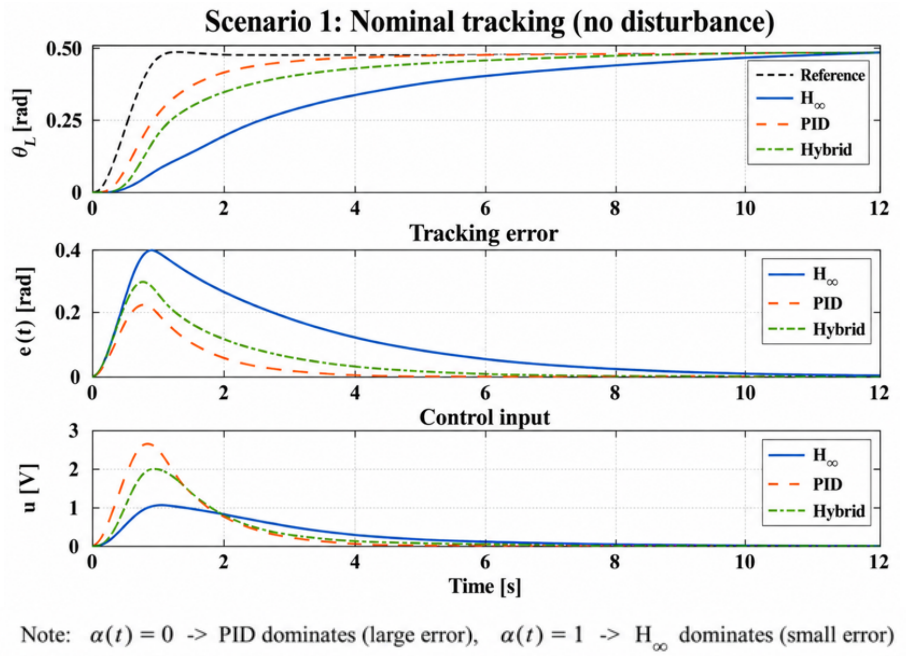

Fig. 12. Nominal tracking performance of the reduced-order joint model (no disturbance)

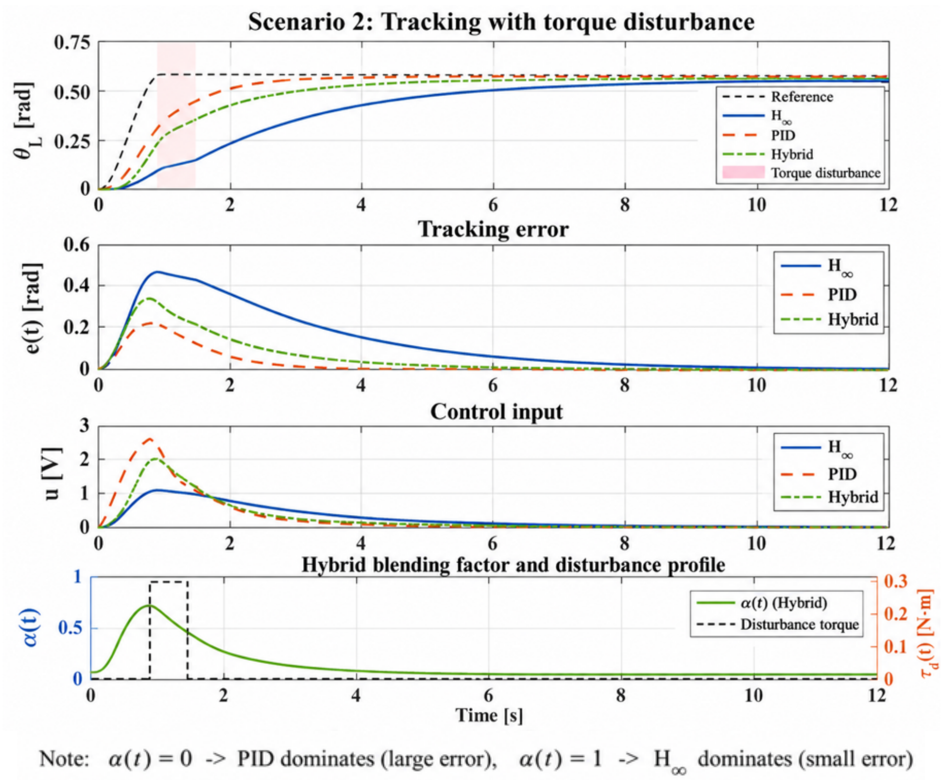

Fig. 13. Tracking performance under a bounded torque disturbance

3.1.3. Performance Metrics under Increasing Disturbance

The time-domain responses shown in Section 3.1.2 show the nominal response to one bounded torque-disturbance case. Table 9 summarizes the RMSE, IAE, and voltage-based control-energy values for Scenario 1 (no disturbance) and Scenario 2 (0.25 N·m torque disturbance). These values were obtained from one deterministic reduced order simulation for each controller and scenario. Therefore, they are used to compare controller trends under identical simulation conditions, not to provide statistical validation.

Table 9. Summary of Tracking Performance and Control Effort for Scenario 1 (Nominal) and Scenario 2 (Torque Disturbance)

Controller	RMSE (S1) $[rad]$	IAE (S1) $[rad \cdot s]$	E_u (S1) $[V^2.s]$	RMSE (S2) $[rad]$	IAE (S2) $[rad \cdot s]$	E_u (S2) $[V^2.s]$
H∞	0.1570	1.2390	1.4048	0.1703	1.3647	1.6514
PID	0.0606	0.3962	4.1708	0.0639	0.4339	4.6203
Hybrid	0.0896	0.5625	3.3527	0.0946	0.6084	3.7534

Table 9 compares the RMSE, IAE, and voltage-based control-energy values for Scenario 1 and Scenario 2. The values were obtained from one deterministic reduced-order simulation for each controller and test condition. Therefore, they are used to compare the response trend of the controllers under the same simulation setup, not to make a statistical claim. The PID controller gives the lowest RMSE and IAE in both scenarios, but it also needs the highest control energy. The *H*∞ controller shows the opposite behavior. It uses the lowest control energy E_u, but its tracking error is larger and the correction is slower. The hybrid *H*∞-PID controller stays between these two responses. This result supports the role of the hybrid controller as a compromise controller, not as the best controller for every metric. Because Scenario 2 uses only one disturbance magnitude, an additional disturbance sweep was also carried out. The maximum disturbance torque $\tau_{\text{dist, max}}$ was varied from 0 to 0.50 N·m with an increment of 0.05 N·m. The same disturbance time window and fixed controller parameters were used for all tests. For each disturbance level, RMSE, IAE, and voltage-based control energy were calculated. This sweep is used as a sensitivity test of the reduced-order model, not as a complete robustness proof for all possible disturbance conditions.

Fig. 14 shows the variation of RMSE as the disturbance amplitude increases. All controllers, RMSE increases as the disturbance torque becomes larger. The PID controller has the smallest RMSE over the tested range, increasing from 0.0606 rad at 0 N·m to approximately 0.067-0.068 rad at 0.50 N·m. The *H*∞ controller has the largest RMSE, increasing from 0.157 rad to approximately 0.184 rad, while the hybrid controller remains between them, increasing from 0.0896 rad to approximately 0.100 rad. Therefore, the disturbance sweep shows a consistent ordering of tracking-error performance for this reduced-order simulation.

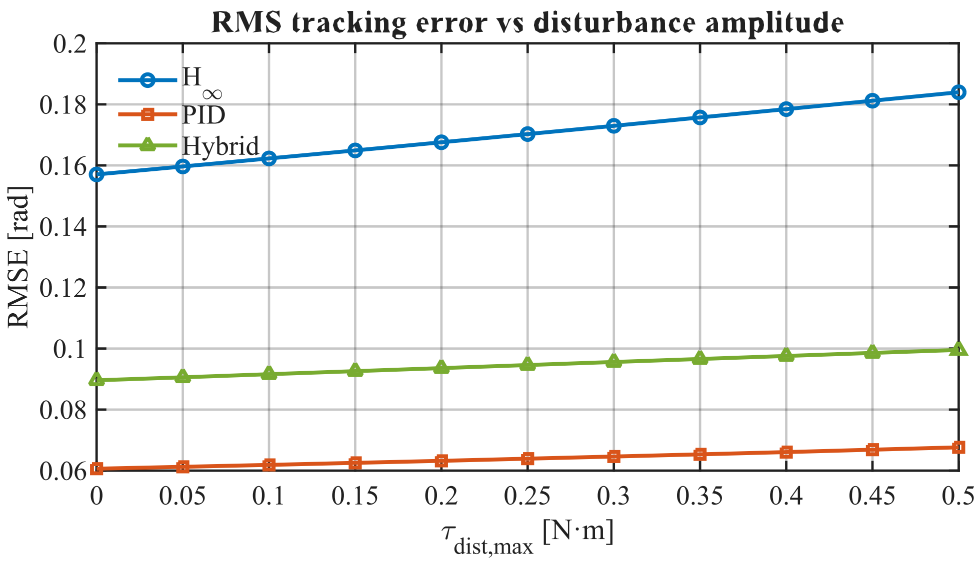

Fig. 14. RMS tracking error versus disturbance amplitude $\tau_{(dist,max)}$

Fig. 15 shows the corresponding IAE trends. The IAE increases with disturbance magnitude for all controllers because the accumulated tracking error becomes larger as the torque disturbance increases. The PID controller gives the lowest IAE, rising from 0.396 rad·s at 0 N·m to about 0.47-0.48 rad·s at 0.50 N·m. The *H∞* controller gives the highest IAE, increasing from 1.239 rad·s to about 1.45 rad·s. The hybrid controller remains between these results, with IAE increasing from 0.563 rad·s to approximately 0.66-0.68 rad·s.

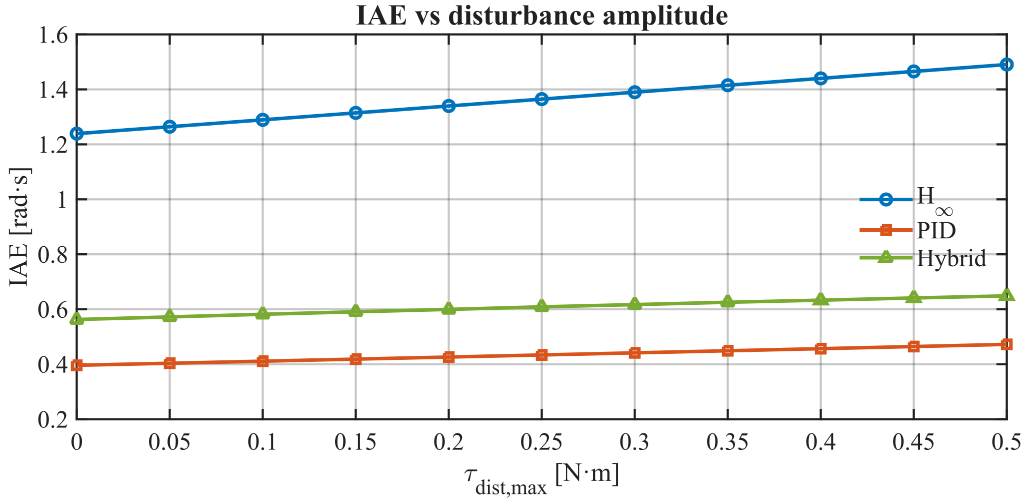

Fig. 15. IAE versus disturbance amplitude $\tau_{(dist,max)}$

The voltage-based control-energy trends are shown in Fig. 16. The control-energy index E_u increases with disturbance magnitude $\tau_{\text{dist, max}}$ for all controllers. The PID controller requires the largest control energy, increasing from 4.17 V^2·s at 0 N·m to about 5.70 V^2·s at 0.50 N·m. The *H∞* controller requires the lowest control energy, increasing from 1.40 V^2·s to about 1.93 V^2·s. The hybrid controller remains between them, increasing from 3.35 V^2·s to about 4.28 V^2·s. This result indicates that lower tracking error in the PID response is obtained with higher voltage demand, while the *H∞* response reduces voltage demand at the cost of slower correction and larger tracking-error metrics.

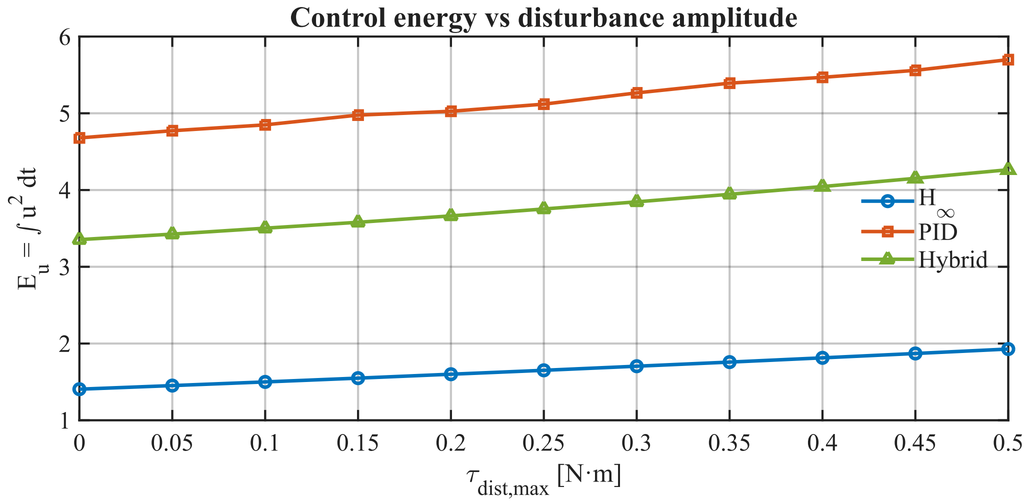

Fig. 16. Control effort index $E_u = \int u^2 (t)dt$ versus disturbance amplitude $\tau_{(dist,max)}$

Overall, the disturbance-amplitude sweep shows a clear trade-off between tracking error and voltage-based control effort. This trend is consistent with constrained manipulator-control studies, where improved tracking performance is often related to higher actuator demand or input saturation handling [67], [68]. In the tested range, the PID controller gives the lowest RMSE and IAE, but it requires the largest actuation demand. The *H∞* controller gives the lowest control energy, but the tracking-error metrics are higher. The hybrid controller does not dominate all metrics. However, it reduces the control demand compared with PID and gives lower accumulated error than *H∞* in the tested simulation. Therefore, the result should be interpreted as a practical trade-off for the reduced-order simulation case, not as statistical evidence that one controller is superior in all conditions.

3.2. Experimental Results

Experimental tests on Joint 3 of the SCORBOT-ER 4U were conducted under practical hardware conditions using the fixed controller parameters described in Section 2.3. Unlike the reduced-order simulations, the hardware responses include physical effects such as friction, backlash, encoder resolution limits, actuator voltage limits, and direction-dependent loading. Similar effects have been reported in manipulator control studies where friction and actuator constraints can degrade tracking accuracy under real operating conditions [69], [70]. Therefore, the experimental results are used to evaluate the controller behavior under practical embedded conditions, not to validate the reduced-order model as a complete representation of the real joint.

Step reference commands of ±10°, ±25°, and ±45° were applied using the same controller parameters and 10 ms sampling period used in the simulation study. The recorded signals include the reference input, measured joint position, and motor-voltage command. The experimental curves in Fig. 17–Fig. 19 are representative responses used to describe the observed time-domain behavior. The responses were checked through repeated trials for qualitative repeatability, but formal statistical confidence intervals were not computed in this study.

Fig. 17 shows the experimental responses for the small step commands of ±10°. For the -10° step in Fig. 17(a), the hybrid controller reaches the reference in about 1.1-1.2 s. The PID controller follows at about 1.2-1.3 s, while the *H∞* controller is slower at about 1.4-1.6 s. The PID response has an overshoot of about 1-2°, while the hybrid response keeps the overshoot below 1° in this representative test. For the +10° step in Fig. 17(b), the response is slower than the -10° case. The three controllers need more than 2 s before the joint stays near the reference. This difference between positive and negative motion shows that the joint response is not fully symmetric. In the hardware test, this condition may come from the combined effect of gravity loading, friction asymmetry, gearbox backlash, and motor-driver dead-zone.

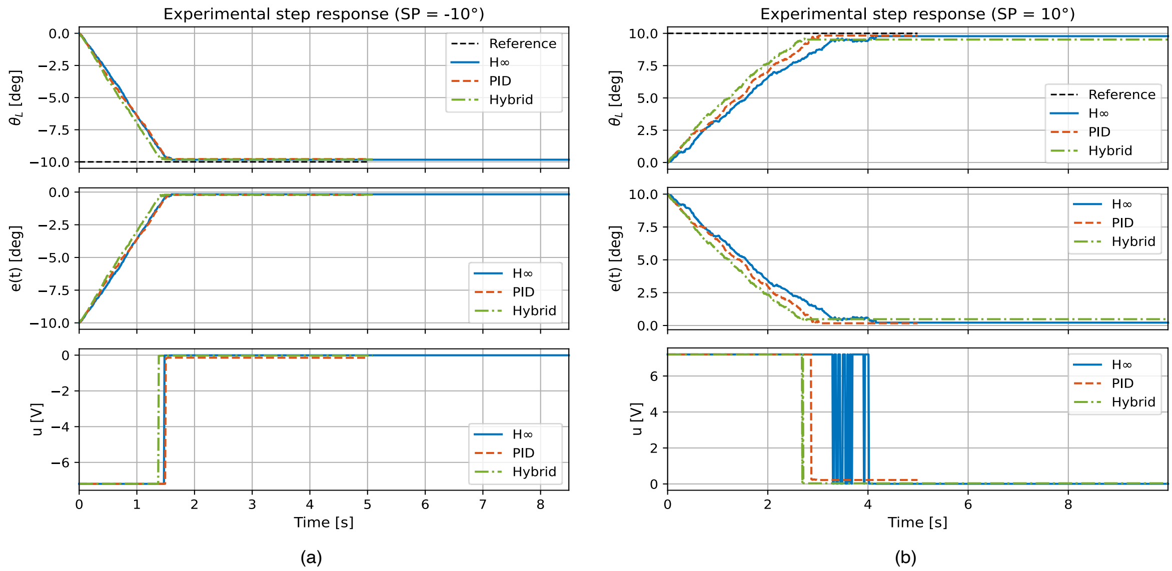

Fig. 17. Tracking performance for small steps (±10°)

Fig. 18 presents the responses for the medium step commands of ±25°. In the -25° test shown in Fig. 18(a), the joint reaches the area near the reference after about 3.5-4 s. In the +25° test shown in Fig. 18(b), the response is slower, and the joint needs around 8-9 s to stay near the reference. This result again shows that the joint does not behave in the same way for both directions. Since gravity, backlash, friction, and dead-zone effects were not identified separately in this work, the asymmetry is treated as a combined hardware effect.

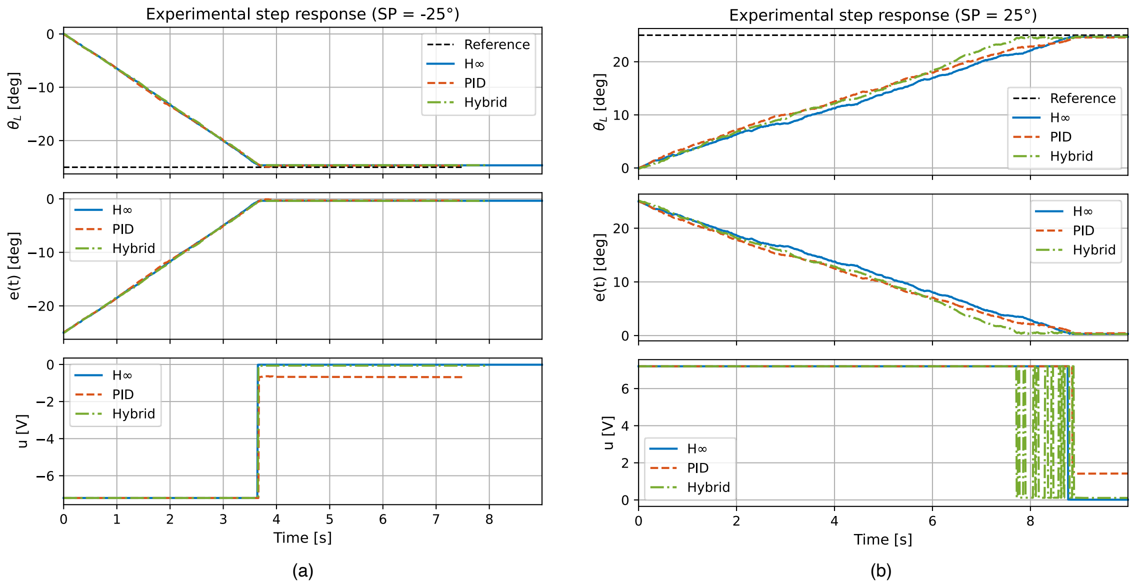

Fig. 18. Tracking performance for medium steps (±25°)

Fig. 19 shows the responses for the large step commands of ±45°. In this test, the joint works closer to the practical limit of the actuator and transmission. For the -45° command in Fig. 19(a), the joint reaches the reference after about 6.5-7 s. For the +45° command in Fig. 19(b), the response is slower and needs around 14-16 s to reach the reference. At the ±45° command, the difference between both directions becomes more visible. The positive step gives a slower correction and shows more oscillation before the joint reaches the reference. This result is reasonable because the joint is working closer to the practical limit of the actuator and transmission. It also shows that the reduced-order model is enough for controller design, but not enough to describe all effects that appear during the hardware test.

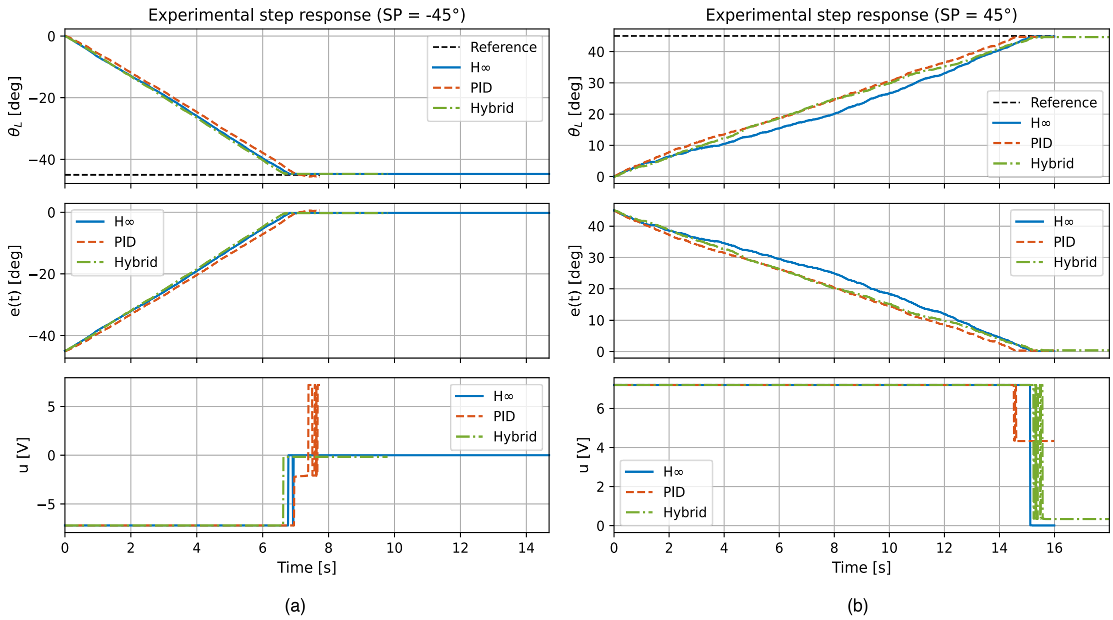

Fig. 19. Tracking performance for large steps (±45°)

Table 10 reports the best controller for each metric in each step test. The same information is shown in Fig. 20 as a heatmap. From these results, the best controller is not always the same. For example, the controller with the lowest RMSE is not always the controller with the lowest IAE or the lowest control-energy value. Therefore, Table 10 should be read as a metric-by-metric comparison of the tested responses, not as proof that one controller is superior in all conditions.

Table 10. Controller Achieving the Lowest Metric Value for Each Step Scenario

Scenario	Best RMSE Controller	Best RMSE Value (°)	Best IAE Controller	Best IAE Value ($° \cdot s$)	Best Energy Controller	Best Energy Value ($V^2 \cdot s$)
SP -45°	$H\infty$	17.87	Hybrid	153.19	Hybrid	343.52
SP -25°	$H\infty$	9.39	PID	48.02	$H\infty$	188.96
SP -10°	$H\infty$	2.53	Hybrid	7.87	Hybrid	71.28
SP 10°	Hybrid	2.86	PID	14.59	Hybrid	139.72
SP 25°	PID	12.68	Hybrid	101.21	Hybrid	424.33
SP 45°	Hybrid	23.49	PID	324.49	PID	781.8

The large-step results also support this interpretation. For the -45° command, the hybrid controller gives the lowest control-energy value of 343.52 $V^2 \cdot s$. For the +45° command, the lowest control-energy value is obtained by the PID controller, with 781.80 $V^2 \cdot s$. This means that the energy result changes with the motion direction. Because the repeated tests were used only to check qualitative repeatability, the RMSE, IAE, and voltage-based control-energy values are reported without mean values, standard deviations, or confidence intervals. Therefore, the comparison is limited to the tested cases and should not be interpreted as formal statistical evidence.

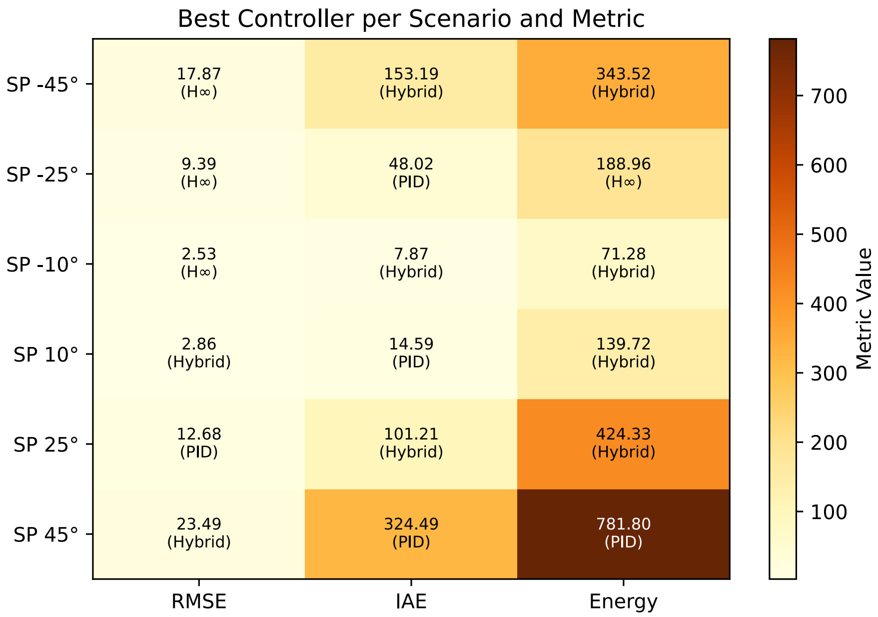

Fig. 20. Heatmap summarizing the best controller per scenario and performance metric

3.3. Comparative Analysis and Discussion

3.3.1. Consistency Between Simulation and Experiment

The simulation and hardware results are not expected to have identical numerical values. The simulation uses a reduced-order joint model, ideal feedback, and predefined disturbance profiles. In the hardware test, the joint response is affected by gearbox backlash, direction-dependent friction, gravity-related loading, encoder quantization, actuator dead-zone, and voltage limits. These factors explain why the experimental error and convergence time are larger than in simulation. Thus, the reduced-order model is used as a design and comparison model, while the hardware test gives the practical response of the real joint.

The difference between positive and negative step responses is also important. The +25° and +45° commands need longer time to converge than the corresponding negative commands. In this study, the effects of gravity, friction, backlash, and motor-driver dead-zone were not separated experimentally. For that reason, the direction-dependent response is considered as a combined hardware nonideality, not as controller instability alone. This interpretation is consistent with previous manipulator-control studies showing that friction, dynamic uncertainty, input saturation [69], [70], gearbox backlash, and transmission effects can reduce tracking accuracy and create delayed correction under real operating conditions [71]–[74].

Fig. 20 and Table 10 show that the best controller changes with the selected metric and operating condition. The PID controller tends to provide faster correction and lower tracking-error metrics in several cases, but this is accompanied by higher voltage-based control energy. The *H*∞ controller tends to reduce control energy but gives slower convergence or larger accumulated error. The hybrid controller is therefore interpreted as an intermediate solution that reduces some undesirable extremes of the stand-alone controllers, rather than as a universally best controller.

The reduced-order model is therefore useful as a controlled reference for comparing fixed controllers under identical simulation conditions. However, the hardware experiments provide the more realistic evaluation of embedded behavior because they include unmodelled nonlinearities and implementation constraints. The agreement between simulation and experiment is qualitative, mainly in the observed trade-off pattern among tracking error, transient behavior, and voltage-based control effort, while the absolute numerical values are expected to differ.

3.3.2. Behavior of the Hybrid Blending Mechanism

The hybrid *H*∞-PID controller uses the error-dependent scheduling mechanism to change the relative contribution of the PID and *H*∞ branches during the transient response. When the tracking error is large, the PID contribution becomes more dominant to provide faster corrective action. As the joint approaches the reference, the *H*∞ contribution becomes more dominant to obtain a smoother response and reduce unnecessary control activity. Therefore, the hybrid controller is not intended to replace the stand-alone controllers in every condition, but to moderate the aggressive response of PID and the slower response of *H*∞ control.

This behavior can be observed in the experimental responses, especially for the large step commands shown in Fig. 19. For the ±45° step responses, the hybrid controller reduces the peak overshoot from approximately 5-7° observed in the more aggressive response to approximately 2-3°. The accumulated metrics in **Error! Reference source not found.** also show that the hybrid controller achieves the lowest IAE or lowest control-energy value in several step scenarios. However, **Error! Reference source not found.** also shows that the hybrid controller does not achieve the best value for every metric. For example, the PID controller still gives the lowest tracking-error metric in some cases, while the *H*∞ controller gives the lowest energy in other cases. This confirms that the hybrid controller should be interpreted as a compromise controller rather than as a universally superior controller.

The use of a continuous error-dependent scheduling mechanism is consistent with hybrid and bumpless-transfer control studies, where smooth transitions are used to reduce abrupt switching between controller actions [57]–[59]. The experimental results also reflect a broader trade-off commonly observed in robotic-control systems, where improved tracking performance must be balanced against actuator demand, robustness, safety constraints, and implementation complexity [75]–[78]. Therefore, controller selection for embedded robotic systems should not be based only on tracking accuracy. Controllers with smaller tracking error may require larger voltage-based control effort, especially under actuator and sampling constraints. In this study, the hybrid controller is interpreted as a practical compromise for reducing overshoot and moderating control effort in several tested conditions, not as a controller that is superior in every metric or operating condition.

3.3.3. Limitations and Scope of Validity

The present study has several limitations that define the scope of validity of the reported results. First, the experimental evaluation is limited to Joint 3 of the SCORBOT-ER 4U and to step-reference inputs of ±10°, ±25°, and ±45°. These tests are useful for observing transient setpoint-tracking behavior, overshoot, and voltage-based control effort, but they do not represent continuous trajectory tracking, coordinated multi-joint motion, or payload-varying manipulation. Further validation using continuous trajectories, payload variations, and multi-joint operation is therefore required before extending the findings to more general robotic motion tasks, especially because trajectory-tracking studies show that motion constraints become more important beyond simple step-response conditions [79], [80]. Future validation should also include calibration-aware evaluation, because industrial robot accuracy can degrade after initial calibration and continuous kinematic calibration has been proposed to maintain positioning accuracy over time [81]. Consequently, the reported RMSE, IAE, and control-energy values should be interpreted as step-response indicators for the tested joint and hardware configuration, not as general motion-quality metrics for all robotic manipulation tasks.

Second, the controllers were designed using a reduced-order joint model that captures the dominant mechanical behavior but does not explicitly model all nonlinear hardware effects. Friction asymmetry, gearbox backlash, gravity-related loading, encoder quantization, actuator dead-zone behavior, and voltage limitations are treated as practical implementation effects observed during hardware testing. The disturbance and parameter-variation analyses are also limited to the selected bounded profiles and reduced-order sensitivity tests. Therefore, the results should not be interpreted as a formal robust-stability proof for the complete nonlinear SCORBOT-ER 4U system.

Third, the experimental trials were repeated to check qualitative repeatability, but formal statistical confidence intervals, standard deviations, and trial-to-trial variability analysis were not computed [82]. The ACS712 current sensor was monitored during testing; however, current-based peak and RMS metrics were not used as primary performance indicators in this paper. A complete per-step metric table including rise time, settling time, steady-state error, peak/RMS voltage, and peak/RMS current was not included because the present analysis focuses on position-tracking indices and voltage-command-based control energy; these metrics will be included in repeated-trial validation in future work. Similarly, detailed real-time profiling of processor load, memory use, and timing jitter on the ESP32-S3 was not included. For this reason, the reported control-effort comparison is limited to the voltage-command-based energy index used consistently across controllers.

Finally, the hybrid $H\infty$-PID controller should be interpreted as a practical compromise controller rather than a universally superior controller. It does not achieve the best value for every metric or every step condition; in some cases, the PID controller gives lower tracking error, while in other cases, the $H\infty$ controller requires lower control energy. The numerical results are specific to the selected PID gains, $H\infty$ weights, hybrid blending parameters, actuator limits, and hardware configuration. Although the blending structure can be transferred conceptually, other joints or robotic platforms would require retuning and further validation.

4. Conclusion

This study evaluated three fixed-parameter controllers for Joint 3 setpoint tracking of the SCORBOT-ER 4U, namely PID, $H\infty$, and hybrid $H\infty$-PID. The comparison was carried out using the same ESP32-S3 controller, 10 ms sampling time, BTS7960 motor driver, encoder feedback, actuator voltage limit, step references, and evaluation metrics. Because of this, the main contribution of the work is the practical comparison of the three controllers under the same embedded hardware condition. The work should not be understood as a new PSO algorithm, a new $H\infty$ synthesis method, or a formal adaptive-control approach.

The simulation results showed that each controller had a different response characteristic. PID produced the lowest tracking error, with RMSE increasing from 0.0606 rad at 0 N·m to around 0.067-0.068 rad at 0.50 N·m. However, this smaller error was obtained with the highest voltage-based control energy, about 5.70 V^2·s at the largest disturbance level. The *H*∞ controller showed the opposite behavior. It required lower control energy, below about 1.93 V^2·s, but its correction was slower and its RMSE and IAE values were higher. The hybrid *H*∞-PID response was located between PID and *H*∞. Therefore, based on the reduced-order simulation, the hybrid controller is better interpreted as a compromise response rather than the best controller for all metrics.

The hardware experiments confirmed that the real joint response was affected by practical nonidealities that were not fully represented in the reduced-order model. These effects include direction-dependent motion, friction, backlash, gravity-related loading, encoder resolution, motor-driver dead-zone, and voltage limitation. In the representative large-step tests, the hybrid controller reduced the peak overshoot from about 5-7° to about 2-3°. However, the best controller was not the same for all cases. PID still gave lower tracking-error values in several tests, while *H*∞ or hybrid control gave lower voltage-based control energy in other tests. This means that controller selection should depend on the operating condition and on which performance criterion is considered more important.

The scope of this work is still limited to fixed-parameter step-response testing on one joint. Multi-joint coordination, continuous trajectory tracking, payload variation, online gain adaptation, formal robust-stability proof for the nonlinear hardware system, current-based energy analysis, processor-load measurement, and statistical repeatability analysis were not included. These points should be addressed in future work. Further testing under broader robotic manipulation conditions is needed before the results can be generalized beyond the tested SCORBOT-ER 4U joint configuration.

Author Contribution: All authors contributed to the conceptualization, implementation, analysis, and manuscript preparation. All authors read and approved the final paper.

Funding: This research was funded by the Sanata Dharma Foundation, Yogyakarta, Indonesia, through research support. The APC was also funded by the Sanata Dharma Foundation.

Acknowledgment: The authors are grateful to the Sanata Dharma Foundation in Yogyakarta, Indonesia, for supporting this research and Rajamangala University of Technology Thanyaburi (RMUTT), Thailand, for supporting the doctoral study and providing research facilities and experimental support.

Conflicts of Interest: The authors declare no conflict of interest.

References

[1] A. Dzedzickis, J. Subačiūtė-Žemaitienė, E. Šutinys, U. Samukaitė-Bubnienė, and V. Bučinskas, "Advanced applications of industrial robotics: New trends and possibilities," *Applied Sciences*, vol. 12, no. 1, Art. no. 135, 2022, https://doi.org/10.3390/app12010135.

[2] A. Sathish Kumar, S. Naveen, R. Vijayakumar, V. Suresh, A. R. Asary, S. Madhu, and P. Kumaran, "An intelligent fuzzy-particle swarm optimization supervisory-based control of robot manipulator for industrial welding applications," *Scientific Reports*, vol. 13, no. 1, Art. no. 8253, 2023, https://doi.org/10.1038/s41598-023-35189-2.

[3] T. Zeng, A. Mohammad, A. G. Madrigal, D. Axinte, and M. Keedwell, "A robust human-robot collaborative control approach based on model predictive control," *IEEE Transactions on Industrial Electronics*, vol. 71, no. 7, pp. 7360–7369, 2024, https://doi.org/10.1109/TIE.2023.3299046.

[4] E. Chávez-Chica, J. Buele, F. W. Salazar, and J. Varela-Aldás, "Prototype system for control the ScorBot ER-4U robotic arm using free tools," in *Advances in Human Factors in Robots, Unmanned Systems and Cybersecurity*, M. Zallio, J. H. Hernandez, and C. R. Ibañez, Eds. Cham, Switzerland: Springer Nature Switzerland AG, 2021, pp. 158–165, https://doi.org/10.1007/978-3-030-79997-7_20.

[5] H. Belgacem, M. Abuabiah, and I. Chihi, "High-fidelity virtual model for industrial robot control under uncertain and disturbed scenarios: A comparative study on the UR5e," *IEEE Access*, vol. 13, pp. 152063–152089, 2025, https://doi.org/10.1109/ACCESS.2025.3604653.

[6] X. Zhang, Y. Wang, X. Yuan, Y. Shen, and Z. Lu, "Adaptive dynamic surface control with disturbance observers for battery/supercapacitor-based hybrid energy sources in electric vehicles," *IEEE Transactions on Transportation Electrification*, vol. 9, no. 4, pp. 5165–5181, 2023, https://doi.org/10.1109/TTE.2022.3194034.

[7] Y. W. Jeong and C. C. Chung, "Observer-based robust control: Its application to permanent magnet synchronous motors," *IEEJ Journal of Industry Applications*, vol. 12, no. 4, pp. 575–587, 2023, https://doi.org/10.1541/ieejjia.22005294.

[8] T. Salzmann, E. Kaufmann, J. Arrizabalaga, M. Pavone, D. Scaramuzza, and M. Ryll, "Real-time neural MPC: Deep learning model predictive control for quadrotors and agile robotic platforms," *IEEE Robotics and Automation Letters*, vol. 8, no. 4, pp. 2397–2404, 2023, https://doi.org/10.1109/LRA.2023.3246839.

[9] L. M. González, "Real-time control systems for embedded robotics applications," *American Journal of Embedded Systems and VLSI Design*, vol. 4, no. 5, pp. 10–14, 2023, https://doi.org/10.71465/ajesvd1300.

[10] Y. Wang, Y. Guan, and H. Li, "Observer-based finite-time sliding-mode control of robotic manipulator with flexible joint using partial states," *International Journal of Intelligent Systems*, vol. 2023, no. 1, Art. no. 8859892, pp. 1–12, 2023, https://doi.org/10.1155/2023/8859892.

[11] Z. Wang, S. Liu, D. Ji, and W. Yi, "Improving real-time performance of Micro-ROS with priority-driven chain-aware scheduling," *Electronics*, vol. 13, no. 9, pp. 1–18, 2024, https://doi.org/10.3390/electronics13091658.

[12] D. Casini, J.-J. Chen, J. Li, F. Reghenzani, and H. Teper, "A survey of real-time support, analysis, and advancements in ROS 2," *Leibniz Transactions on Embedded Systems*, vol. 11, no. 1, Art. no. 1, pp. 1:1–1:37, 2026, https://doi.org/10.4230/LITES.11.1.1.

[13] T. Yaren and S. Kizir, "Real-time nonlinear model predictive control of a robotic arm using spatial operator algebra theory," *Journal of Field Robotics*, vol. 42, no. 5, pp. 2337–2354, 2025, https://doi.org/10.1002/rob.22514.

[14] R. Chen, "A comprehensive analysis of PID control applications in automation systems: Current trends and future directions," *Highlights in Science, Engineering and Technology*, vol. 97, pp. 126–132, 2024, https://doi.org/10.54097/6q4xxg69.

[15] L. Cavanini, F. Ferracuti, and A. Monteriù, "Optimal error governor for PID controllers," *International Journal of Systems Science*, vol. 52, no. 12, pp. 2480–2492, 2021, https://doi.org/10.1080/00207721.2021.1890272.

[16] A. Eltayeb, G. Ahmed, I. H. Imran, N. M. Alyazidi, and A. Abubaker, "Comparative analysis: Fractional PID vs. PID controllers for robotic arm using genetic algorithm optimization," *Automation*, vol. 5, no. 3, pp. 230–245, 2024, https://doi.org/10.3390/automation5030014.

[17] Y. Wang, Z. Wang, L. Zou, and H. Dong, "H∞ PID control for discrete-time fuzzy systems with infinite-distributed delays under round-robin communication protocol," *IEEE Transactions on Fuzzy Systems*, vol. 30, no. 6, pp. 1875–1888, 2022, https://doi.org/10.1109/TFUZZ.2021.3069329.

[18] H. Kızmaz, "Comparative analysis of optimal control strategies: LQR, PID, and sliding mode control for DC motor position performance," *Gazi University Journal of Science Part A: Engineering and Innovation*, vol. 10, no. 4, pp. 571–592, 2023, https://doi.org/10.54287/gujsa.1393092.

[19] D. Ravikumar and G. K. Srinivasan, "Implementation of higher order sliding mode control of DC–DC buck converter fed permanent magnet DC motor with improved performance," *Automatika*, vol. 64, no. 1, pp. 162–177, 2023, https://doi.org/10.1080/00051144.2022.2119499.

[20] M. Boussoffara, I. B. C. Ahmed, and Z. Hajaiej, "Sliding mode controller design: Stability analysis and tracking control for flexible joint manipulator," *Revue Roumaine des Sciences Techniques — Série Électrotechnique et Énergétique*, vol. 66, no. 3, pp. 161–167, 2021, https://journal.iem.pub.ro/rrst-ee/en/article/view/26/17.

[21] P. Schwerdtner and M. Voigt, "Fixed-order H-infinity controller design for port-Hamiltonian systems," *Automatica*, vol. 152, Art. no. 110918, 2023, https://doi.org/10.1016/j.automatica.2023.110918.

[22] K. Lu, G. Feng, and B. Ding, "Robust H-infinity tracking control for a valve-controlled hydraulic motor system with uncertain parameters in the complex load environment," *Sensors*, vol. 23, no. 22, Art. no. 9092, 2023, https://doi.org/10.3390/s23229092.

[23] K. Vinida and M. Chacko, "Implementation of speed control of sensorless brushless DC motor drive using H-infinity controller with optimized weight filters," *International Journal of Power Electronics and Drive Systems*, vol. 12, no. 3, pp. 1379–1389, 2021, https://doi.org/10.11591/ijpeds.v12.i3.pp1379-1389.

[24] M. Ali and H. Mirinejad, "Robust tracking control of flexible manipulators using hybrid backstepping/nonlinear reduced-order active disturbance rejection control," *ISA Transactions*, vol. 149, pp. 229–236, 2024, https://doi.org/10.1016/j.isatra.2024.04.026.

[25] R. Rojas-Galván, J. A. Romero-Moreno, R. V. Carrillo-Serrano, J. R. García-Martínez, T. Martínez-Sánchez, M. Trejo-Perea, J. G. Ríos-Moreno, and J. Rodríguez-Reséndiz, "A classic and fuzzy parallel hybrid controller of PD-PI type for a two-wheeled self-balancing robot," *Automation*, vol. 7, no. 2, Art. no. 49, 2026, https://doi.org/10.3390/automation7020049.

[26] G. Ahmed, A. Eltayeb, N. M. Alyazidi, I. H. Imran, T. Sheltami, and S. El-Ferik, "Improved particle swarm optimization for fractional order PID control design in robotic manipulator system: A performance analysis," *Results in Engineering*, vol. 24, Art. no. 103089, 2024, https://doi.org/10.1016/j.rineng.2024.103089.

[27] F. Z. Baghli, Y. Lakhal, and Y. A. El Kadi, "The efficiency of an optimized PID controller based on ant colony algorithm (ACO-PID) for the position control of a multi-articulated system," *Journal of Robotics and Control (JRC)*, vol. 4, no. 3, pp. 289–298, 2023, https://doi.org/10.18196/jrc.v4i3.17709.

[28] E. S. Rahayu, A. Ma'arif, and A. Cakan, "Particle swarm optimization (PSO) tuning of PID control on DC motor," *International Journal of Robotics and Control Systems*, vol. 2, no. 2, pp. 435–447, 2022, https://doi.org/10.31763/ijrcs.v2i2.476.

[29] E. H. Houssein, M. K. Saeed, G. Hu, and M. M. Al-Sayed, "Metaheuristics for solving global and engineering optimization problems: Review, applications, open issues and challenges," *Archives of Computational Methods in Engineering*, vol. 31, no. 8, pp. 4485–4519, 2024, https://doi.org/10.1007/s11831-024-10168-6.

[30] A. G. Gad, "Particle swarm optimization algorithm and its applications: A systematic review," *Archives of Computational Methods in Engineering*, vol. 29, no. 5, pp. 2531–2561, 2022, https://doi.org/10.1007/s11831-021-09694-4.

[31] M. H. Setiawan, A. Ma'arif, M. F. Saifuddin, and W. A. Salah, "A comparative study of PID, FOPID, ISF, SMC, and FLC controllers for DC motor speed control with particle swarm optimization," *International Journal of Robotics and Control Systems*, vol. 5, no. 1, pp. 640–660, 2025, https://doi.org/10.31763/ijrcs.v5i1.1764.

[32] S. Charkoutsis and M. Kara-Mohamed, "A particle swarm optimization tuned nonlinear PID controller with improved performance and robustness for first order plus time delay systems," *Results in Control and Optimization*, vol. 12, Art. no. 100289, 2023, https://doi.org/10.1016/j.rico.2023.100289.

[33] L. Zhao and T. Wu, "Design and robust control of a dual-loop valve-controlled cylinder system," *Results in Engineering*, vol. 27, Art. no. 106515, 2025, https://doi.org/10.1016/j.rineng.2025.106515.

[34] M. S. Ahmed, A. H. M. Mary, and H. H. Jasim, "Robust computed torque control for uncertain robotic manipulators," *Al-Khwarizmi Engineering Journal*, vol. 17, no. 3, pp. 22–28, 2021, https://doi.org/10.22153/kej.2021.09.002.

[35] Y.-L. Yeh, "A robust noise-free linear control design for robot manipulator with uncertain system parameters," *Actuators*, vol. 10, no. 6, Art. no. 121, 2021, https://doi.org/10.3390/act10060121.

[36] A. T. Bankole and E. E. C. Igbonoba, "Simulation-based novel hybrid proportional derivative/H-infinity controller design for improved trajectory tracking of a two-link robot arm," *Journal of Shanghai Jiaotong University (Science)*, vol. 30, no. 6, pp. 1179–1187, 2025, https://doi.org/10.1007/s12204-023-2660-5.

[37] R. Zhang, Z. Wang, and P. Keogh, "H-infinity optimised control of external inertial actuators for higher precision robotic machining," *International Journal of Computer Integrated Manufacturing*, vol. 35, no. 2, pp. 129–144, 2022, https://doi.org/10.1080/0951192X.2021.1972467.

[38] P. Sutyasadi and M. Parnichkun, "Push recovery control of quadruped robot using particle swarm optimization based structure specified mixed sensitivity H2/H∞ control," *Industrial Robot*, vol. 47, no. 3, pp. 423–434, 2020, https://doi.org/10.1108/IR-06-2019-0135.

[39] P. Sutyasadi and M. B. Wicaksono, "Joint control of a robotic arm using particle swarm optimization based H2/H∞ robust control on Arduino," *TELKOMNIKA (Telecommunication Computing Electronics and Control)*, vol. 18, no. 2, pp. 1021–1029, 2020, https://doi.org/10.12928/telkomnika.v18i2.14749.

[40] B. Alizadeh, A. Hajipour, H. Tavakoli, and A. Nasrabadi, "Robust trajectory tracking of delta parallel robot using fractional-order sliding mode control," *IEEE Access*, vol. 11, pp. 86397–86412, 2023, https://doi.org/10.1109/ACCESS.2023.3302525.

[41] M. B. Wicaksono, D. Maneetham, and P. Sutyasadi, "Hybrid adaptive control for robotic arm using PID-ILC approach," *Engineering, Technology and Applied Science Research*, vol. 15, no. 6, pp. 29002–29012, 2025, https://doi.org/10.48084/etasr.13495.

[42] Y. Hu, S. Dian, R. Guo, S. Li, and T. Zhao, "Observer-based dynamic surface control for flexible-joint manipulator system with input saturation and unknown disturbance using type-2 fuzzy neural network," *Neurocomputing*, vol. 436, pp. 162–173, 2021, https://doi.org/10.1016/j.neucom.2020.12.121.

[43] A. Al-Tamimi, F. Al-Momani, M. Salah, S. Banihani, and A. Al-Jarrah, "Control strategies for DC motor systems driving nonlinear loads in mechatronic applications," *Actuators*, vol. 15, no. 3, Art. no. 175, 2026, https://doi.org/10.3390/act15030175.

[44] N. M. Tung, V. T. K. Nhi, and D. Q. Tuan, "Reduced-order dynamic modeling for a DC motor coupled with flywheel and torsion shaft using the eigenmode truncation method," *Journal of Robotics and Control*, vol. 6, no. 3, pp. 1264–1272, 2025, https://doi.org/10.18196/jrc.v6i3.26459.

[45] K. Xu, X. Wu, X. Liu, and D. Wang, "Identification of robot joint torsional stiffness based on the amplitude of the frequency response of asynchronous data," *Machines*, vol. 9, no. 9, Art. no. 204, 2021, https://doi.org/10.3390/machines9090204.

[46] X. Zhang and Y. Yang, "Optimization of PID controller parameters using a hybrid PSO algorithm," *International Journal of Dynamics and Control*, vol. 12, no. 10, pp. 3617–3627, 2024, https://doi.org/10.1007/s40435-024-01455-y.

[47] C. Wang, Z. Wang, F. Han, H. Dong, and H. Liu, "A novel PID-like particle swarm optimizer: On terminal convergence analysis," *Complex & Intelligent Systems*, vol. 8, no. 2, pp. 1217–1228, 2022, https://doi.org/10.1007/s40747-021-00589-2.

[48] F. Wang, K. Chen, S. Zhen, X. Chen, H. Zheng, and Z. Wang, "Prescribed performance adaptive robust control for robotic manipulators with fuzzy uncertainty," *IEEE Transactions on Fuzzy Systems*, vol. 32, no. 3, pp. 1318–1330, 2024, https://doi.org/10.1109/TFUZZ.2023.3323090.

[49] J. Ma, Z. Cheng, H. Zhu, X. Li, M. Tomizuka, and T. H. Lee, "Convex parameterization and optimization for robust tracking of a magnetically levitated planar positioning system," *IEEE Transactions on Industrial Electronics*, vol. 69, no. 4, pp. 3798–3809, 2022, https://doi.org/10.1109/TIE.2021.3070518.

[50] S. Xu, Z. Wu, and T. Shen, "High-precision control of industrial robot manipulator based on extended flexible joint model," *Actuators*, vol. 12, no. 9, Art. no. 357, 2023, https://doi.org/10.3390/act12090357.

[51] X. Ning, "Mixed sensitivity-based robust H∞ control method for real-time hybrid simulation," *Symmetry*, vol. 13, no. 5, Art. no. 840, 2021, https://doi.org/10.3390/sym13050840.

[52] P. Schuchert and A. Karimi, "Frequency-domain data-driven position-dependent controller synthesis for Cartesian robots," *IEEE Transactions on Control Systems Technology*, vol. 31, no. 4, pp. 1855–1866, 2023, https://doi.org/10.1109/TCST.2023.3257487.

[53] M. Indri, M. Bellissimo, S. Pesce, and V. Perna, "A robust H∞ application for motor-link control systems of industrial manipulators," *Applied Sciences*, vol. 12, no. 17, Art. no. 8890, 2022, https://doi.org/10.3390/app12178890.

[54] A. Moutsopoulou, M. Petousis, N. Vidakis, G. E. Stavroulakis, and A. Pouliezos, "Applications of the order reduction optimization of the H-infinity controller in smart structures," *Inventions*, vol. 8, no. 6, Art. no. 150, 2023, https://doi.org/10.3390/inventions8060150.

[55] G. I. Song, H. Y. Park, and J. H. Kim, "The H∞ robust stability and performance conditions for uncertain robot manipulators," *IEEE/CAA Journal of Automatica Sinica*, vol. 12, no. 1, pp. 270–272, 2025, https://doi.org/10.1109/JAS.2024.124701.

[56] N. T. Chung and C. H. Tinh, "Design of robust H∞ combined with PID controller using fuzzy logic for a missile autopilot," *Advances in Military Technology*, vol. 19, no. 1, pp. 41–53, 2024, https://doi.org/10.3849/aimt.01831.

[57] V. B. Nguyen and X. C. Bui, "Hybrid vibration control algorithm of a flexible manipulator system," *Robotics*, vol. 12, no. 3, Art. no. 73, 2023, https://doi.org/10.3390/robotics12030073.

[58] W. Chen, Y. Shi, and Z. Fei, "Time and switching signal scheduled bumpless transfer control for switched systems with application to aero-engines," *Nonlinear Analysis: Hybrid Systems*, vol. 48, Art. no. 101327, 2023, https://doi.org/10.1016/j.nahs.2022.101327.

[59] X. Song and J. Lam, "Bumpless H∞ control for periodic piecewise linear systems," *Automatica*, vol. 135, Art. no. 109941, 2022, https://doi.org/10.1016/j.automatica.2021.109941.

[60] X. Zhang, S. Xiong, and R. Guo, "Robust bumpless transfer control for switched systems with unmatched uncertainties based on the common robust integral sliding mode under arbitrary switching rules," *Mathematics*, vol. 12, no. 22, Art. no. 3504, 2024, https://doi.org/10.3390/math12223504.

[61] Y. Shi, J. Zhao, and X. M. Sun, "A bumpless transfer control strategy for switched systems and its application to an aero-engine," *IEEE Transactions on Industrial Informatics*, vol. 17, no. 1, pp. 52–62, 2021, https://doi.org/10.1109/TII.2020.2979736.

[62] M. R. Liu, Z. Wu, X. Du, and Z. Fei, "Finite-time and bumpless transfer control of asynchronously switched systems: An output feedback control approach," *Journal of the Franklin Institute*, vol. 361, no. 3, pp. 1566–1581, 2024, https://doi.org/10.1016/j.jfranklin.2024.01.026.

[63] J. Fu, X. Liu, Y. Liu, Z. Chen, and B. Yao, "Fast and accurate tracking control of robotic manipulators subject to state constraints and input saturation by effectively integrating planning strategies," *ISA Transactions*, vol. 149, pp. 373–380, 2024, https://doi.org/10.1016/j.isatra.2024.04.012.

[64] R. Zhang, Z. Wang, N. Bailey, and P. Keogh, "Experimental assessment and feedforward control of backlash and stiction in industrial serial robots for low-speed operations," *International Journal of Computer Integrated Manufacturing*, vol. 36, no. 3, pp. 393–410, 2023, https://doi.org/10.1080/0951192X.2022.2090609.

[65] J. A. G. L. Junior, J. M. Balthazar, M. A. Ribeiro, F. C. Janzen, and A. M. Tusset, "Dynamic model of a robotic manipulator with one degree of freedom with friction component," *International Journal of Robotics and Control Systems*, vol. 3, no. 2, pp. 315–329, 2023, https://doi.org/10.31763/ijrcs.v3i2.984.

[66] J. Moreno-Valenzuela, G. Zepeda, R. Rascón, M. Moran-Armenta, and J. Moyrón, "An SLF approach to trajectory tracking control of input-restricted robot manipulators," *Control Engineering Practice*, vol. 165, Art. no. 106533, 2025, https://doi.org/10.1016/j.conengprac.2025.106533.

[67] B. Li, H. Zhan, X. Zhang, and C. Yang, "Single-network based adaptive dynamic programming optimal control for robotic manipulator with joint limitation under input saturation," *International Journal of Systems Science*, vol. 55, no. 16, pp. 3355–3370, 2024, https://doi.org/10.1080/00207721.2024.2370301.

[68] T. Wang, F. Wang, Z. Xie, and F. Qin, "Curiosity model policy optimization for robotic manipulator tracking control with input saturation in uncertain environment," *Frontiers in Neurorobotics*, vol. 18, Art. no. 1376215, 2024, https://doi.org/10.3389/fnbot.2024.1376215.

[69] W. Lyu, D. H. Zhai, Y. Xiong, and Y. Xia, "Predefined performance adaptive control of robotic manipulators with dynamic uncertainties and input saturation constraints," *Journal of the Franklin Institute*, vol. 358, no. 14, pp. 7142–7169, 2021, https://doi.org/10.1016/j.jfranklin.2021.07.025.

[70] Y. Sun, X. Liang, and Y. Wan, "Tracking control of robot manipulator with friction compensation using time-delay control and an adaptive fuzzy logic system," *Actuators*, vol. 12, no. 5, Art. no. 184, 2023, https://doi.org/10.3390/act12050184.

[71] E. Giovannitti, S. Nabavi, G. Squillero, and A. Tonda, "A virtual sensor for backlash in robotic manipulators," *Journal of Intelligent Manufacturing*, vol. 33, no. 7, pp. 1921–1937, 2022, https://doi.org/10.1007/s10845-022-01934-z.

[72] L. Sun and H. Gu, "Backlash elimination control for robotic joints with dual-motor drive," *Actuators*, vol. 13, no. 8, Art. no. 291, 2024, https://doi.org/10.3390/act13080291.

[73] M. Pollák, M. Kočiško, S. D. Grozav, V. Ceclan, and A. D. Bogdan, "Suitability of UR5 robot for robotic 3D printing," *Applied Sciences*, vol. 14, no. 21, Art. no. 9845, 2024, https://doi.org/10.3390/app14219845.

[74] B. Yang and X. Jing, "Spatial error prediction and compensation of industrial robots based on extended joints and BO-XGBoost," *Sensors*, vol. 25, no. 20, Art. no. 6422, 2025, https://doi.org/10.3390/s25206422.

[75] M. Salman, Z. Niu, R. Singh, L. Kshetrimayum, and I. Hussain, "Robust control of a compliant manipulator with reduced dynamics and sliding perturbation observer," *Scientific Reports*, vol. 15, no. 1, Art. no. 8934, 2025, https://doi.org/10.1038/s41598-025-91904-1.

[76] S. Mustary, M. A. Kashem, J. M. Sony, N. Hossain, and M. Asaduzzaman Chowdhury, "Advancing stability in robot manipulators: A review of recent progress and parameters," *Engineering Reports*, vol. 7, no. 7, Art. no. e70207, 2025, https://doi.org/10.1002/eng2.70207.

[77] J. Sandoval, R. Kelly, V. Santibáñez, and J. Villalobos-Chin, "Energy regulation of torque-driven robot manipulators in joint space," *Journal of the Franklin Institute*, vol. 359, no. 4, pp. 1427–1456, 2022, https://doi.org/10.1016/j.jfranklin.2022.01.034.

[78] Q. Nguyen and K. Sreenath, "Robust safety-critical control for dynamic robotics," *IEEE Transactions on Automatic Control*, vol. 67, no. 3, pp. 1073–1088, 2022, https://doi.org/10.1109/TAC.2021.3059156.

[79] H. Wang, X. Li, X. Fan, J. Liu, L. Wei, and Y. Tie, "Dynamic modeling and trajectory tracking control of a flexible joint robotic manipulator considering gear friction torque excitation," *Advances in Space Research*, vol. 77, no. 1, pp. 828–852, 2026, https://doi.org/10.1016/j.asr.2025.10.015.

[80] X. Li, X. Gao, and K. Zhang, "Safe trajectory tracking for robotic manipulator with prescribed performance in confined spaces," *Symmetry*, vol. 18, no. 1, Art. no. 2, 2025, https://doi.org/10.3390/sym18010002.

[81] G. Qiao, X. Jiang, M. Zhang, C. Gao, and Y. Zhang, "A continuous kinematic calibration method for accuracy maintenance of industrial robot based on recursive least squares algorithm," *Scientific Reports*, vol. 15, no. 1, Art. no. 11397, 2025, https://doi.org/10.1038/s41598-025-95523-8.

[82] A. Faragasso and F. Bonsignorio, "Reproducibility challenges in robotic surgery," *Frontiers in Robotics and AI*, vol. 10, Art. no. 1127972, 2023, https://doi.org/10.3389/frobt.2023.1127972.